iScience

CellPress
OPEN ACCESS

Article

Long-working-distance high-collection-efficiency three-photon microscopy for *in vivo* long-term imaging of zebrafish and organoids

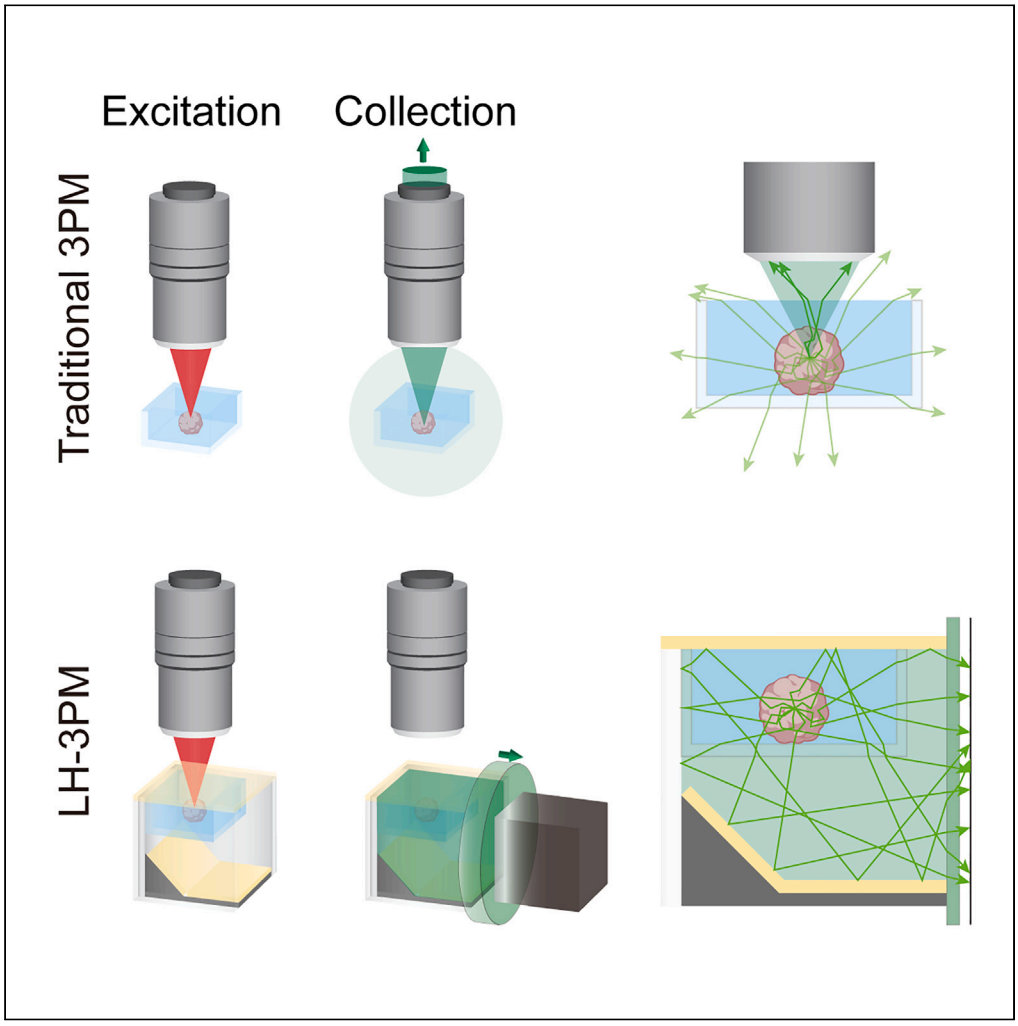

Peng Deng, Shoupei Liu, Yaoguang Zhao, ..., Zhicheng Shao, Cihang Kong, Bo Li

zcshao@fudan.edu.cn (Z.S.)
kongcihang@fudan.edu.cn (C.K.)
bo_li@fudan.edu.cn (B.L.)

Highlights

LH-3PM introduces a groundbreaking non-contact, non-intrusive multiphoton imaging method

LH-3PM achieves a 15-fold increase in photon collection efficiency and improves signal

LH-3PM reduces photobleaching rates by more than 700-fold and phototoxic effects

LH-3PM demonstrates enhanced capability to capture neuronal activity

Deng et al., iScience 27, 110554
August 16, 2024
https://doi.org/10.1016/j.isci.2024.110554

iScience

CellPress
OPEN ACCESS

Article

Long-working-distance high-collection-efficiency three-photon microscopy for *in vivo* long-term imaging of zebrafish and organoids

Peng Deng,[1,7] Shoupei Liu,[1,7] Yaoguang Zhao,[1,7] Xinxin Zhang,[2] Yufei Kong,[3] Linlin Liu,[3] Yujie Xiao,[1] Shasha Yang,[4] Jiahao Hu,[1] Jixiong Su,[1] Ang Xuan,[1,5] Jinhong Xu,[3] Huijuan Li,[3] Xiaoman Su,[6] Jingchuan Wu,[4] Yuli Jiang,[1] Yu Mu,[2] Zhicheng Shao,[3,*] Cihang Kong,[1,*] and Bo Li[1,8,*]

SUMMARY

Zebrafish and organoids, crucial for complex biological studies, necessitate an imaging system with deep tissue penetration, sample protection from environmental interference, and ample operational space. Traditional three-photon microscopy is constrained by short-working-distance objectives and falls short. Our long-working-distance high-collection-efficiency three-photon microscopy (LH-3PM) addresses these challenges, achieving a 58% fluorescence collection efficiency at a 20 mm working distance. LH-3PM significantly outperforms existing three-photon systems equipped with the same long working distance objective, enhancing fluorescence collection and dramatically reducing phototoxicity and photobleaching. These improvements facilitate accurate capture of neuronal activity and an enhanced detection of activity spikes, which are vital for comprehensive, long-term imaging. LH-3PM's imaging of epileptic zebrafish not only showed sustained neuron activity over an hour but also highlighted increased neural synchronization and spike numbers, marking a notable shift in neural coding mechanisms. This breakthrough paves the way for new explorations of biological phenomena in small model organisms.

INTRODUCTION

In the fields of biology and medical research, zebrafish and organoids have become key models for understanding complex biological processes and disease mechanisms.[1,2] The optical transparency and rapid growth cycle of zebrafish, along with the ability of organoids to replicate the three-dimensional structures characteristic of humans, make them indispensable in studies of developmental biology,[3] neurobiology,[4] and pathology.[5] Particularly, optical methods for dynamic and real-time imaging of these models provide an unprecedented window into complex biological phenomena.[6,7] This is especially crucial in studying neurological disorders like epilepsy,[8,9] where capturing the rapid and complex dynamics is necessary for understanding the pathology.[10] The unique properties of these model organisms pose specific demands on the optical imaging techniques. Firstly, their typically millimeter-scale size requires an imaging system with strong depth penetration capabilities.[11] Secondly, they have strict requirements for their culture conditions, necessitating maximum isolation from external disturbances and contamination.[12] Thirdly, as zebrafish and organoids may be located at different depths within the culture medium, the imaging system must be able to clearly capture samples at both shallow and deeper layers.[13] Lastly, the imaging system needs to reserve sufficient space to integrate additional experimental equipment, such as micromanipulators,[14] electrodes,[15] and constant temperature heaters,[16] essential for certain experiments.

Recent advancements in three-photon microscopy (3PM) have achieved significant breakthroughs in increasing penetration depth.[17–21] For example, traditional two-photon microscopy (2PM) was limited to imaging juvenile zebrafish and challenging for less transparent adult zebrafish.[22–25] Instead, Joseph R. Fetcho's research group used 3PM to pioneer full-brain imaging of adult zebrafish.[26] This innovative method

[1]Department of Neurosurgery, Huashan Hospital, MOE Frontiers Center for Brain Science, State Key Laboratory of Medical Neurobiology, Institutes for Translational Brain Research, Fudan University, Shanghai 200032, China
[2]Institute of Neuroscience, State Key Laboratory of Neuroscience, Center for Excellence in Brain Science and Intelligence Technology, Chinese Academy of Sciences, Shanghai 200031, China
[3]Institute for Translational Brain Research, State Key Laboratory of Medical Neurobiology, MOE Frontiers Center for Brain Science, Institute of Pediatrics, National Children's Medical Center, Children's Hospital, Fudan University, Shanghai 200032, China
[4]Department of Neurosurgery, Huashan Hospital, Fudan University, Shanghai 200032, China
[5]Academy for Engineering and Technology, Fudan University, Shanghai 200433, China
[6]State Key Laboratory of Medical Neurobiology, Institutes of Brain Science, MOE Frontiers Center for Brain Science, Department of Neurology of Zhongshan Hospital, Fudan University, Shanghai 200032, China
[7]These authors contributed equally
[8]Lead contact
*Correspondence: zcshao@fudan.edu.cn (Z.S.), kongcihang@fudan.edu.cn (C.K.), bo_li@fudan.edu.cn (B.L.)
https://doi.org/10.1016/j.isci.2024.110554

allowed them to capture spontaneous calcium activities in neurons up to 750 μm beneath the head's surface while maintaining a high signal-to-noise ratio (SNR). In the field of organoid imaging, the imaging depth of 2PM is limited to about 300 μm, making it impossible to observe the structure and function of the deep organoids.[27] Mriganka Sur's research group broke this limit with 3PM, successfully imaging organoids up to 2 mm deep.[28] However, despite these advances in depth penetration, current 3PM systems still fall short in fulfilling three specific imaging requirements for zebrafish and organoids. Due to the lower fluorescence excitation probability of 3PM, they require very high fluorescence collection efficiency. As a result, objectives with high numerical aperture (NA) and short working distance are commonly employed, such as water immersion objectives with an NA of 1.05 and a working distance of 2 mm, which are prevalent in most research.[29–33] Therefore, fulfilling the ideal imaging requirements for zebrafish and organoids is extremely challenging.

To avoid contamination and to provide a larger imaging range and more operational space, researchers have traditionally used long working distance objectives.[34–37] Objectives mediated by air can prevent direct contact between the microscope and the sample, thus avoiding contamination.[38] Long working distance objectives can image samples at various depths in solution and provide more operational space.[39] However, due to the physical limitations of optical design, these objectives have a small fluorescence collection angle and low NA, leading to low fluorescence collection efficiency.[40–44] For example, ideally, a 0.4 NA, 20-mm long working distance air objective has a fluorescence collection efficiency of only 4%, whereas a 1.05 NA, 2-mm short working distance water immersion objective can achieve a 19% collection efficiency, as shown in Figure 1C. When fluorescence collection efficiency is low, higher excitation power is needed to capture images of sufficient SNR. This increase in excitation power can lead to photobleaching and phototoxicity, which are detrimental for long-term live imaging.[13,45]

To address these trade-offs, we developed a long-working-distance high-collection-efficiency three-photon microscopy (LH-3PM) to meet the imaging needs of zebrafish and organoids. Our system achieves a fluorescence collection efficiency of up to 58% at a 20 mm working distance, even exceeding the efficiency of high NA objectives by three times in theory. Compared to traditional 3PM systems with similar long working distances, our method improves fluorescence signal collection by more than 15 times, significantly decreasing photobleaching rates by over 700 times and reducing phototoxicity. It can capture neuronal activity more effectively and record a higher number of activity spikes, which is beneficial for long-term live imaging. Using LH-3PM, we conducted live imaging of epileptic zebrafish for an hour and observed no significant increase in the number of highly active neurons, but an increase in the degree of synchronization between neurons and the average number of activity spikes, suggesting a shift in neural coding.

RESULTS

Principle of LH-3PM

The success of multiphoton microscopy largely hinges on its ability to efficiently collect fluorescence.[29] Therefore, optimization of fluorescence collection pathway is a critical aspect of multiphoton microscope design.[42,43,46] In developing our LH-3PM, we focused on improving the collection efficiency to enhance deep tissue imaging. Before optimization, we examined the fluorescence collection demands unique to both 2PM and 3PM. Our simulations, depicted in Figure 1A, reveal the differences in fluorescence distribution within 1 mm thick biological tissues when using two-photon and three-photon excitation.

The fluorescence generation and distribution are governed by the excitation intensity. Due to scattering and absorption, the excitation light experiences attenuation as it travels through tissue.[29,47] However, the focusing nature of the objective lens causes laser intensity to intensify with depth. In this case, multiphoton microscopes generate fluorescence at the focal point through nonlinear effects. Yet, when imaging at greater depths, two-photon excitation also produces off-focus excitation, leading to significant background noise. In contrast, three-photon excitation minimizes this issue.

By analyzing the signal-to-background ratio (SBR) across depths (Figure 1B), this difference can be more clearly identified. With increasing depth, the SBR in 2PM decreases rapidly. At about 500–600 μm, the SBR reaches a point where signal and noise are equivalent (SBR = 0 dB), making effective imaging impossible. In 3PM, however, the SBR remains high even at 1 mm depth, indicating its superiority in deep tissue imaging. For 2PM, increasing fluorescence collection efficiency also amplifies background noise, which can affect the signal quality in deeper regions.[42–44,46,48] Here, reducing background noise is more crucial than merely enhancing fluorescence collection.[49] For 3PM the goal is to capture as much fluorescence as possible from the focal point, enhancing overall imaging performance.[34]

In traditional 3PM systems, a single objective is utilized both for focusing the laser onto the sample (Figure 1C left) and collecting the emitted fluorescence.[17,18,20,26,28,30,31,47] However, this configuration captures only a limited fraction of the fluorescence at the focal point, as most of the fluorescence photons are emitted in multiple directions within the biological tissue (Figure 1C right). This results in relatively low photon collection efficiency. The issue is further compounded in samples with high scattering properties, where even more fluorescence signal is lost (Figure 1D). Ideally, the maximum collection efficiency achievable for objectives with an NA of 0.4 and 1.05 is 4% and 19%, respectively (Figure 1E). However, at a depth of 1 mm, tissue scattering further diminishes this efficiency, making deep tissue imaging more challenging (Figure 1F).

Our LH-3PM addressed these limitations by separating fluorescence excitation and collection. We retained a long working distance objective for sample excitation (Figure 1G left) and introduced a light-reflecting chamber for collecting fluorescence (Figure 1G right). The light-reflecting chamber is primarily composed of mirrors and long-pass filters (Figure S2 and Video S1). The long-pass filter at the top allows the transmission of excitation light to excite the sample. When the sample inside the chamber is excited, it emits photons in all directions. The signal light that hits the chamber's side walls is reflected by vertically placed mirrors and a 45-degree inclined long-pass filter toward the detector. Similarly, signal light emitted toward the top and bottom of the chamber is also reflected by the long-pass filters positioned at the top

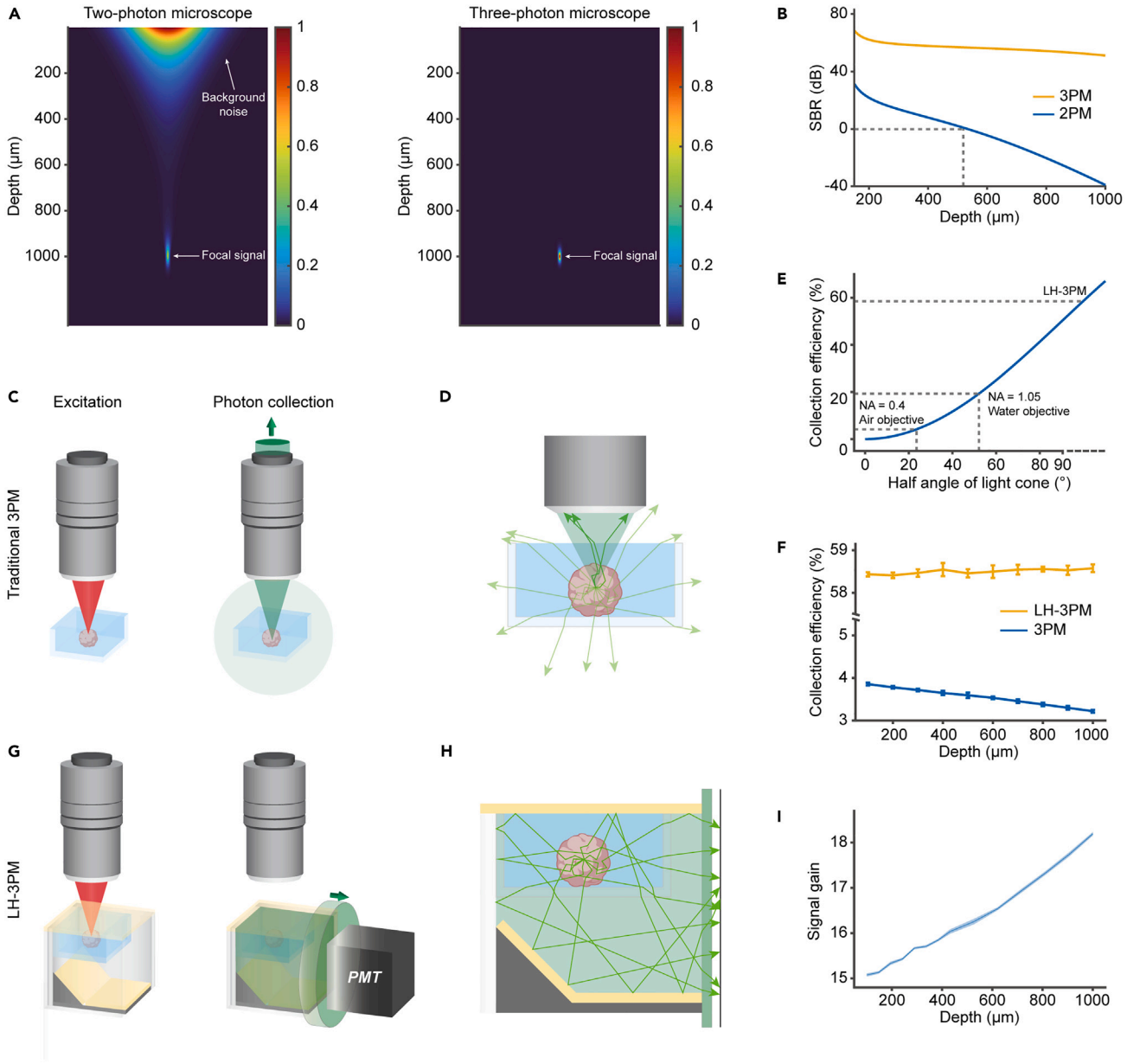

Figure 1. Principle of LH-3PM

(A) Simulation of fluorescence distribution under two-photon and three-photon excitation through 1 mm thick scattering biological tissue. Both can generate strong fluorescence signals at the focus. Nevertheless, two-photon excitation also produces significant background noise, which is not observed in three-photon excitation.

(B) The curves showing the SBR of 2PM and 3PM versus imaging depth.

(C) Concept of fluorescence excitation and collection of traditional 3PM.

(D) Ray-tracing diagram of scattered photons collected by a long working distance objective.

(E) Idealized plot of the theoretical collection efficiency of an objective versus the half angle of the light cone.

(F) Simulation curve showing photon collection efficiency versus imaging depth for traditional 3PM with 0.4 NA air objective and LH-3PM at an emission wavelength of 520 nm. We used mean ± SEM here. $n = 6$ simulation results for each depth.

(G) Concept of fluorescence excitation and collection in LH-3PM.

(H) Ray-tracing diagram of scattered photons collected by LH-3PM. The yellow parts represent the long pass filters, and the white parts represent the reflective mirrors.

(I) The curve showing the signal enhancement gain of LH-3PM relative to traditional 3PM with 0.4 NA air objective versus imaging depths at an emission wavelength of 520 nm.

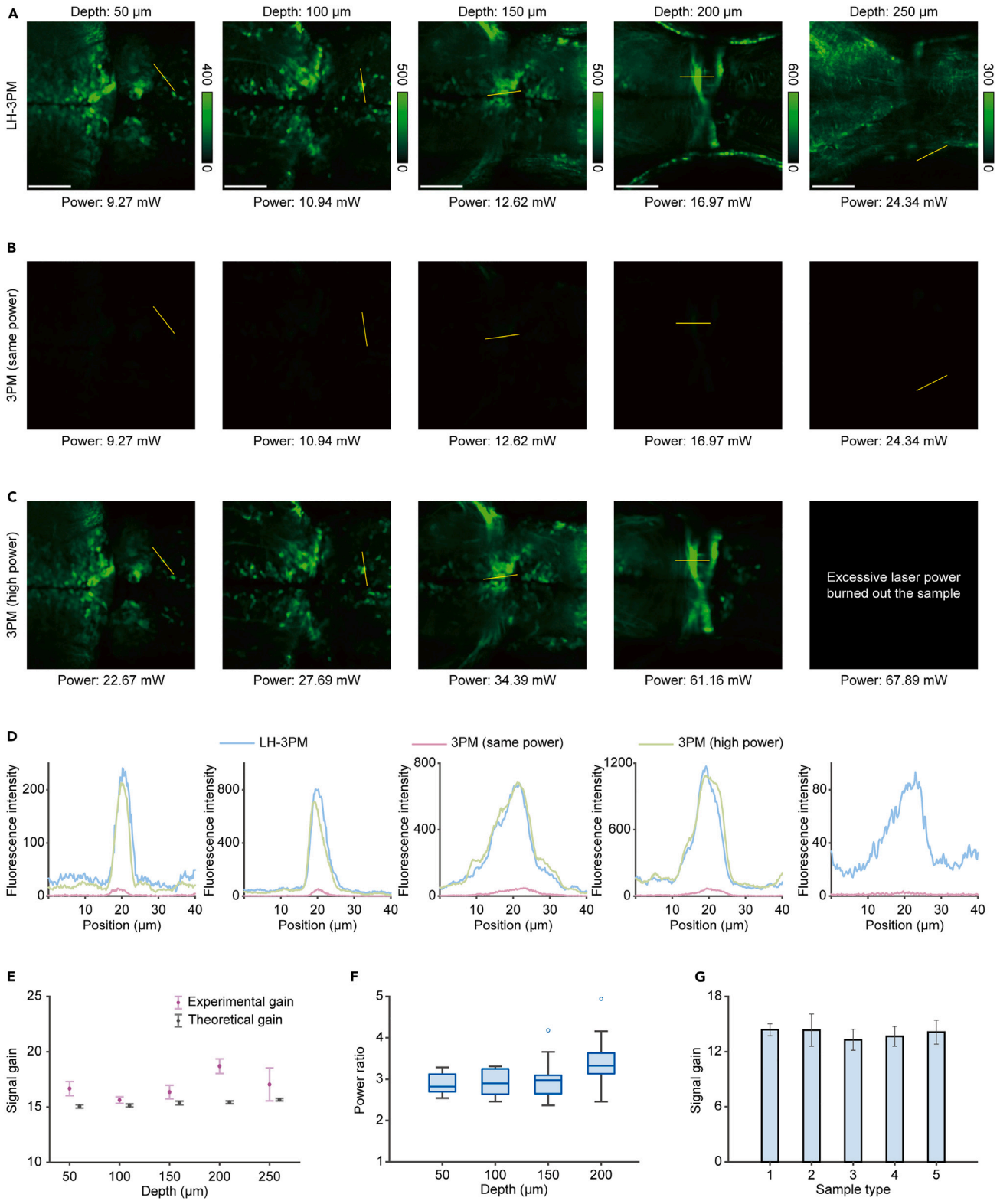

Figure 2. LH-3PM facilitates deep penetration comparable with traditional 3PM

(A) Imaging results of the mGreenLantern-labeled neurons in the zebrafish brain obtained at different depths by LH-3PM. All excitation powers marked at the bottom are measured at the objective output.

Figure 2. *Continued*

(B) Imaging results of the mGreenLantern-labeled neurons in the zebrafish brain obtained at different depths by traditional 3PM. The excitation power at different depths is the same as that in (A). The color bar of the image is the same as that of the corresponding depth in (A).

(C) Imaging results of the mGreenLantern-labeled neurons in the zebrafish brain obtained at different depths by traditional 3PM with high powers. All excitation powers marked at the bottom are measured at the objective output. The color bar of the image is the same as that of the corresponding depth in (A).

(D) Fluorescence intensity profiles along the yellow lines indicated in (A), (B), and (C). To produce each plot, a five-pixel-wide line was drawn across the cell body. The 5-pixel values were averaged to get an intensity value for the corresponding position along the line.

(E) Curves of simulation prediction gain and measured signal enhancement strength versus imaging depth for mGreenLantern-labeled neurons of zebrafish (n = 5 neurons or simulation results for each depth). We used mean ± SEM here.

(F) The ratio of excitation power used by LH-3PM–3PM under the same photon counts obtained (n = 10 neurons for each depth). We used mean ± SEM here.

(G) Measured signal enhancement strength of LH-3PM compared to 3PM in different samples. From left to right, the samples are GFP-labeled mouse brain neuron, GFP-labeled mouse brain microglia, mouse brain blood vessels with THG, cortical organoid rosette structure with THG and zebrafish skin surface with THG (n = 5 imaging regions for each sample). We used mean ± SEM here.

See also Figure S5. Scale bars: 50 μm.

and bottom toward the detector (Figure S9E). This design significantly enhances the microscope's ability to collect signal light. Even in highly scattering samples, LH-3PM efficiently captures signal photons (Figure 1H). We optimized the chamber's design through simulations (Figures S1D and S1E) and achieved a photon collection efficiency of 58%, which is unaffected by imaging depth (Figure 1F). Compared to traditional microscopy methods, LH-3PM demonstrates a significant improvement in efficiency—over 15 times higher for a 0.4 NA 20-mm working distance objective and 3 times higher for a 1.05 NA 2-mm working distance objective in theory (Figures 1E and 1I).

Signal enhancement characterization of LH-3PM

To evaluate the enhanced signal capabilities of our LH-3PM, we performed comparative imaging of zebrafish neurons labeled with mGreenLantern. Both traditional 3PM and LH-3PM were employed across varying imaging depths, followed by a quantitative analysis of the results. Using identical power settings, LH-3PM consistently produced brighter and more distinct images at all depths when compared to traditional 3PM (Figures 2A and 2B). We marked identical regions within the imaging area and quantified the fluorescence intensity. The results, as shown by the blue and red lines in Figure 2D, indicated a notable enhancement in signal brightness with LH-3PM. Further quantitative comparison of the same neuronal structures captured by both methods revealed that LH-3PM enhanced fluorescence signals by over 15-fold across all depths, aligning with our simulation analyses (Figure 2E).

In addition, traditional 3PM could match the fluorescence signal intensity of LH-3PM by increasing the excitation power. We conducted a parallel study at different depths, adjusting the excitation power of traditional 3PM to match the fluorescence signal of LH-3PM (Figures 2A and 2C). The fluorescence intensity curves, marked by red and green lines in Figure 2D, showed near-identical signal strengths in both methods. We then segmented the same neuronal structures and calculated the power ratio required to produce equivalent fluorescence intensities. Traditional 3PM necessitated 2.5 to 4 times the excitation power of LH-3PM for similar fluorescence signal (Figure 2F). This finding highlights LH-3PM's higher collection efficiency. It can capture comparable images with significantly lower laser power and thereby reduce potential photobleaching or photodamage, which is especially critical for long-term imaging.

Moreover, LH-3PM was equally effective in imaging cortical organoids, as demonstrated through third harmonic signal (THG) imaging of cell and ventricular zone-like structures (Figure S4). LH-3PM's applicability was demonstrated by imaging various biological samples, including mouse brain slices with GFP-labeled neurons, GFP-labeled microglia, blood vessels (using THG), and zebrafish skin structures (using THG) (Figure S5). Statistical analyses corroborate that LH-3PM, with the same excitation power, enhances performance by approximately 15 times compared to traditional 3PM equipped with the same long working distance objective (Figure 2G).

LH-3PM reduces photodamage during long-term imaging

Furthermore, the advanced capabilities of LH-3PM not only achieved imaging enhancement, but also minimized photodamage during long-term imaging using long working distance objective. Photobleaching and phototoxicity are significant concerns in live imaging,[50] where long-term or high-intensity light exposure can diminish the fluorescence ability of molecules (photobleaching) and potentially harm biological samples (phototoxicity).

We have confirmed that the signal collection efficiency is improved by more than 15 times via optical simulation and biological experiments. This means that, when the signals collected by both methods are essentially the same, the actual fluorescence intensity generated by the traditional 3PM is more than 15 times that of the LH-3PM. Since photobleaching is a complex nonlinear process and typically exhibits exponential decay, LH-3PM reduces photobleaching more significantly than the 15-fold increase in fluorescence collection efficiency suggests.

Thus, we further characterized the photobleaching effects of the two imaging methods. In a comparative study, we used LH-3PM and traditional 3PM to image the same mouse brain region containing GFP-labeled neurons continuously over 36 min. Both methods were initially set to exhibit similar fluorescence intensities to assess the extent of photobleaching. The neurons marked with yellow arrows in LH-3PM images maintained consistent brightness over time, while those in traditional 3PM images exhibited a gradual decrease in fluorescence, indicating significant photobleaching (Figures 3A and 3B; Video S2).

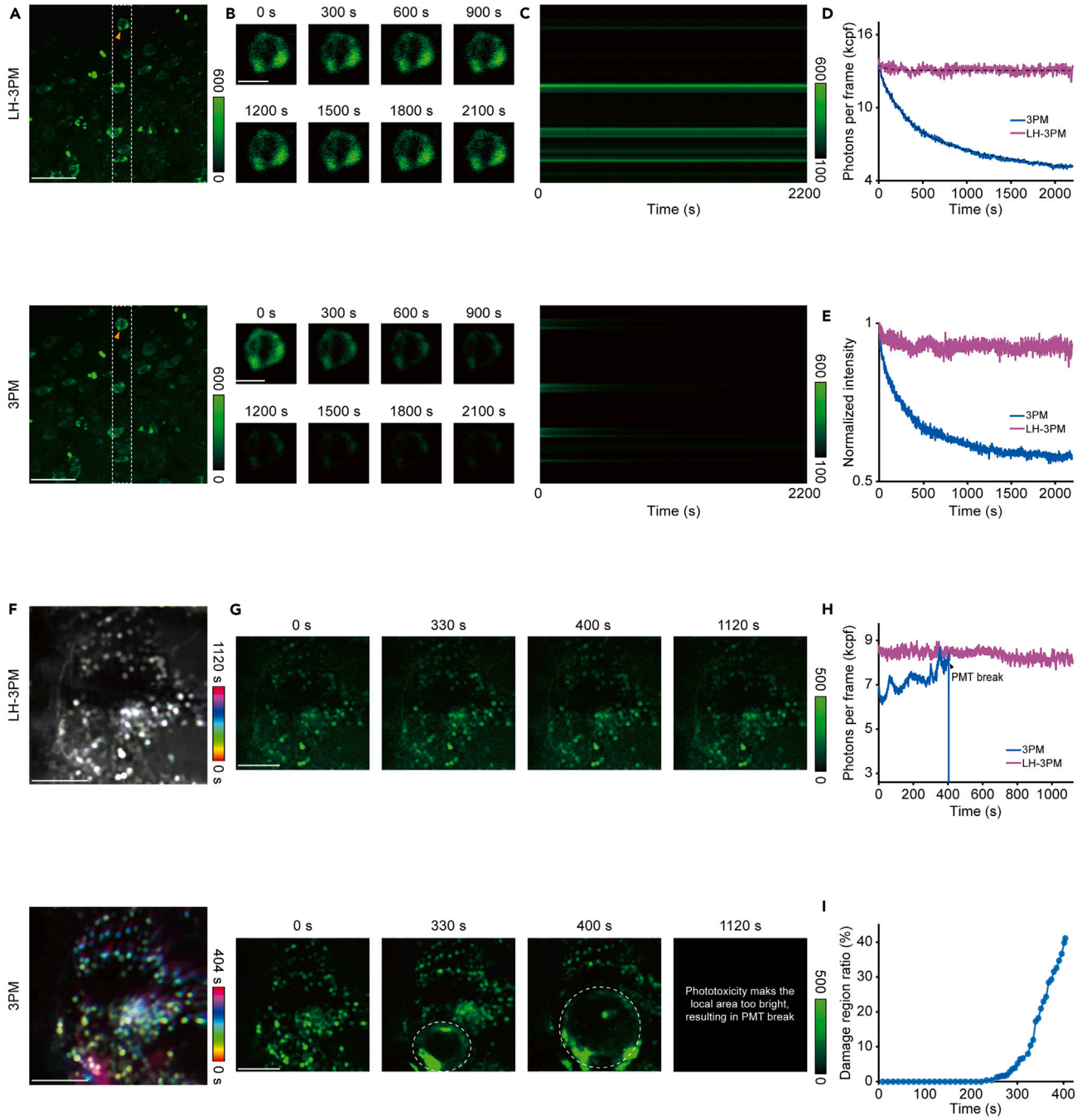

Figure 3. LH-3PM reduces photobleaching and phototoxicity of traditional 3PM during long-term imaging

(A) Initial image of GFP-labeled neurons in mouse brain slice imaged by LH-3PM and 3PM. The power measured at the objective output for LH-3PM was 12.94 mW. The power measured at the objective output for 3PM was 31.47 mW.

(B) The brightness changes of the neuron indicated by the yellow arrow in (A) over time. The color bar of the image is the same as that in (C).

(C) The brightness changes of the white dashed-line region indicated in (A) over time captured by LH-3PM and 3PM.

(D) Curve of photon counts of neurons that can be segmented in each frame versus time in LH-3PM and 3PM. The dashed lines in the graph represent the curves obtained through exponential fitting.

(E) Curve of normalized fluorescence intensity of the white dashed-line region versus time in LH-3PM and 3PM.

(F) Average intensity projection images of long-term imaging of GCaMP7f-labeled zebrafish neurons using LH-3PM and 3PM. The power measured at the objective output for LH-3PM was 14.85 mW. The power measured at the objective output for 3PM was 34.91 mW. The color bar indicates the elapsed imaging time.

Figure 3. *Continued*

(G) Images captured at different imaging points by LH-3PM and 3PM.

(H) Curve of photon counts in each frame versus time in LH-3PM and 3PM.

(I) Curve of the ratio of the damage region versus time in long-term imaging by 3PM. Scale bars: 50 μm in (A), (F), and (G) and 10 μm in (B).

Quantitative analysis of photon counts in identifiable neurons across frames revealed a marked contrast. Photon counts of neurons in LH-3PM images remained nearly constant, whereas traditional 3PM showed an exponential decay in photon counts over time (Figure 3D). This finding was further substantiated by analyzing fluorescence intensity changes over time in a specific area (Figure 3C). Curves of normalized fluorescence intensity illustrated that the signal from LH-3PM remained stable, while traditional 3PM experienced a pronounced exponential decrease (Figure 3E). By fitting these decay curves, we calculated photobleaching rate constants and revealed that LH-3PM's photobleaching rate was reduced by over 700 times compared to traditional 3PM equipped with the same long working distance objective.

In addition to photobleaching, phototoxicity is a critical concern in live imaging.[51] Phototoxicity refers to the damage inflicted on biological samples due to light exposure.[52] Reducing phototoxicity is essential to prevent cell damage and maintain the normal physiological environment of biological samples, ensuring the accuracy and reliability of experimental results.[53] We utilized LH-3PM for long-term imaging of zebrafish neurons labeled with GCaMP7f and compared it with traditional 3PM. Initial excitation fluorescence photon counts were similar for both methods. Over time, LH-3PM images were clearer and more stable, with no significant cell displacement. In contrast, traditional 3PM resulted in distorted cell images and formation of bubble-like damage structures, indicative of phototoxicity (Figure 3F; Video S3).

Displaying images at specific time points allows us to show that LH-3PM provided stable, undistorted images, while traditional 3PM showed severe structural distortion and damage, including bubble formation caused by high laser power (Figure 3G). Quantitative analysis of these long-term recorded videos confirmed the stability of fluorescence photon counts with LH-3PM, in contrast to the fluctuations and sudden drops due to photodamage-triggered overbrightness in traditional 3PM. We conducted area statistics on the bubble-like structure and found that the damaged area appeared and expanded rapidly during traditional 3PM imaging (Figure 3I). This expansion was exponential, indicating a rapid onset of photodamage.

In summary, the enhanced performance of LH-3PM not only provides superior imaging quality but also significantly reduces photodamage, including both photobleaching and phototoxicity. This makes it an invaluable tool for long-term live imaging studies, where sample integrity and minimal interference with biological processes are crucial.[50]

Functional imaging characterization of LH-3PM

In the characterization of LH-3PM, we also focused on its functional imaging capabilities. Specifically, we compared LH-3PM and traditional 3PM by performing *in vivo* calcium imaging for zebrafish. This assessment was crucial to demonstrate the practical utility of LH-3PM in capturing dynamic biological processes.

Imaging was performed on the same brain region across multiple zebrafishes with GCaMP7f-labeled neurons (5 days post-fertilization, n = 3), capturing a series of 20-min time-lapse images. As displayed in Figure 4A, the resulting average projection images revealed a distinct contrast. LH-3PM captured distinct neuronal structures with clarity, which were not discernible with traditional 3PM.

We extracted calcium signals from seven neurons within the image region and normalized these signals against fluorescence baseline (Figures 4B and 4C). The calcium signal curves acquired by LH-3PM exhibited a notably higher SNR, characterized by more pronounced and distinct peaks, which suggests heightened sensitivity and clarity in functional imaging. Further, we analyzed calcium signals from five neurons shown in Figure 4A and quantified the fluorescence photon count for each frame (Figures 4D and 4E). The comparison of the fluorescence baseline photon counts revealed that LH-3PM achieved an average photon count (mean ± SEM = 184.82 ± 16.40) over eight times higher than that of traditional 3PM (mean ± SEM = 22.15 ± 5.54), as depicted in Figure 4F.

Moreover, when comparing the average peak fluorescence photon counts recorded by both LH-3PM and traditional 3PM, LH-3PM (mean ± SEM = 247.32 ± 20.47) consistently yielded a value more than seven times higher than traditional 3PM (mean ± SEM = 31.25 ± 6.60), as shown in Figures 4G and S6B. This enhancement in both baseline and peak fluorescence intensities facilitated a more accurate identification of cellular activity spikes within the time-lapse images.

To further substantiate these findings, we employed Suite2p, a widely used toolkit for live neural calcium imaging.[54] After applying Suite2p for cell segmentation and spike signal extraction from videos recorded via both imaging methods, we found that LH-3PM recorded a significantly higher number of effective cells, approximately four times that of traditional 3PM (Figures 4H and S6A). Additionally, LH-3PM extracted a higher average number of spike activities per neuron (mean 1130.1) compared to traditional 3PM (mean 905.7), as illustrated in Figures 4I and S6C.

These comprehensive results demonstrate that LH-3PM is not only superior for live calcium imaging by providing higher SNR videos, but it also effectively captures more detailed spike activities from each neuron. This advanced functional imaging capability of LH-3PM is pivotal for neurological studies, particularly those requiring long-term observation of live specimens.[45]

PTZ-induced zebrafish seizure calcium activity visualized by LH-3PM

Epilepsy is a chronic neurological disorder characterized by abnormal neuronal discharges in the brain, which can lead to a range of symptoms, including loss of consciousness, muscle spasms, sensory abnormalities, or changes in mental state.[55,56] The high vertebrate relevance, relatively transparent brains, and rapid growth cycles of zebrafish make them a valuable model for simulating human epileptic seizures.[22,57,58]

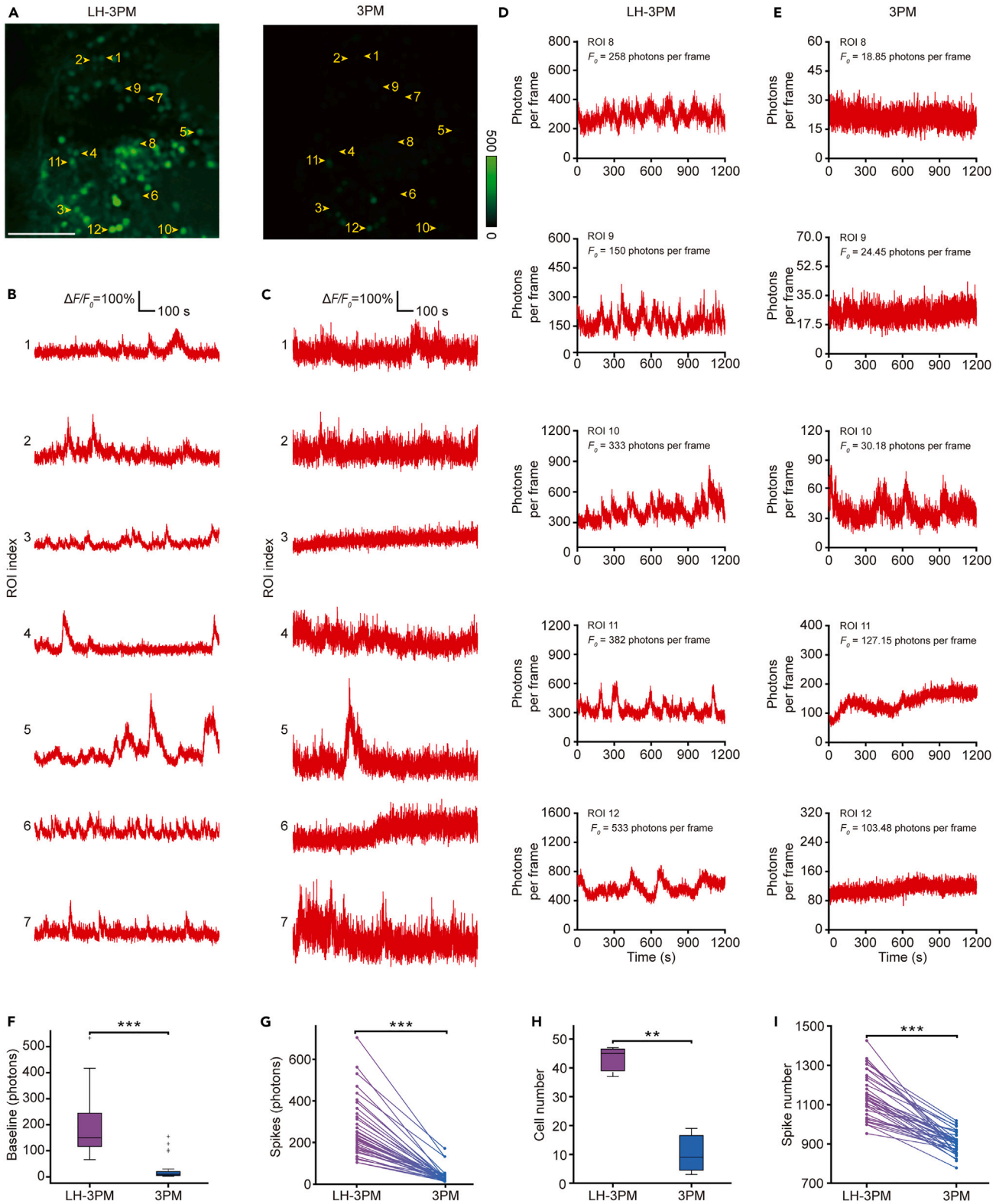

Figure 4. Comparison of spontaneous neuronal activity captured by LH-3PM and 3 PM at the same location in an anesthetized zebrafish

(A) Average intensity projection images of neurons with LH-3PM and 3PM. The neurons are located at 250 μm beneath the skull and labeled with the GCaMP7f. (B and C) Spontaneous activity traces recorded from the labeled neurons indicated in (A) with LH-3PM (B) and with 3PM (C).

Figure 4. *Continued*

(D and E) Quantitative photon counting of the activity traces of the neurons recorded from the labeled neurons indicated in (A) with LH-3PM (D) and with 3PM (E).

(F) Bar plots of baseline photon counts of spontaneous activity traces from neurons imaged by LH-3PM and 3PM respectively (n = 40 neurons). We used mean ± SEM here.

(G) Average spike fluorescence intensity of spontaneous activity traces from neurons imaged by LH-3PM and 3PM respectively. Each line represents 1 of 40 calcium traces.

(H) Bar plots of cell segmentation numbers based on spontaneous activity traces by LH-3PM and 3PM, respectively. We used mean ± SEM here.

(I) Spike number of spontaneous activity traces from neurons imaged by LH-3PM and 3PM respectively (n = 40 neurons). Statistical significance was determined using one-way ANOVA with the Dunnett's multiple comparisons test. $^{**}p < 0.01$; $^{***}p < 0.001$. Scale bars, 50 μm. F, fluorescence intensity; F_0, baseline fluorescence; ΔF, F- F_0.

In our study, we used pentylenetetrazole (PTZ), a central nervous system stimulant known to induce epileptic seizures by inhibiting the function of GABA receptors.[59] This reduction in GABA-mediated inhibitory neurotransmission causes neuronal excitation and synchronous discharge.

Using LH-3PM, we performed live calcium imaging on zebrafish for up to 1 h, with the addition of PTZ at a specified time point during imaging (Figure 5A). This approach allowed for continuous recording before, during, and after the epileptic seizures. Initially, we created average projections from videos taken before and during the seizures (Figures 5B and 5C). Post-seizure, the images showed an increased number of brightened neurons, indicating a highly active state of neuronal activity.

We extracted and analyzed the calcium activities of 110 neurons during the imaging process. By binarizing these activities using three times the SEM as a threshold, we observed an increase in neuronal calcium activity following PTZ induction, with large-scale synchronous discharge behavior emerging in the later stages (Figures 5C and S7; Video S4).

The progression of the epileptic seizures was further characterized by plotting changes in the number of significantly active cells, average fluorescence intensity, and spike count per frame (Figure 5D). As the seizures developed, the number of significantly active neurons exhibited oscillatory changes, indicating a tendency toward synchronized discharges. At certain moments, more neurons discharged simultaneously, while at other times, the number of simultaneously discharging neurons was less than before the seizure. The average fluorescence intensity of cells increased rapidly after seizure induction, and interestingly, rather than a continuous increase, the intensity showed significant spikes at specific moments. The spike count trend mirrored the fluorescence intensity pattern.

To quantify the synchronization degree of neuronal discharges, we calculated the time-dependent average discharge rates and $\Delta F/F_0$ pairwise correlation coefficients for each pair of cells (n = 7140 pairs) and compared these coefficients before and after seizures (Figure 5E). Post-seizure, the average discharge rate correlation and $\Delta F/F_0$ correlation of neurons increased significantly (the average discharge rate correlation pre-seizure: mean ± SEM = 0.0008 ± 0.0004, post-seizure: mean ± SEM = 0.22 ± 0.002, and $\Delta F/F_0$ pre-seizure: mean ± SEM = 0.03 ± 0.0032, post-seizure: mean ± SEM = 0.41 ± 0.003, $p < 0.0001$). This indicated a substantial increase in the degree of synchronization between neurons following the seizure.

Finally, we analyzed the neural coding mechanisms before and after the seizures using the CEBRA algorithm.[60] The coding mechanisms of all neurons were analyzed over time (Figure 5F). Before the seizure, the coding mode of the neuronal population was stable and resembled a closed-loop circle. As the seizures progressed, the coding mode deviated from this circular structure and shifted to more irregular shape. During intensified seizure periods, the neuronal population activities showed significant clustering at specific moments, suggesting highly correlated neural network activities and synchronized neuronal discharges. These moments of clustering in the neural coding visualization corresponded to the moments of transient changes in calcium activity-related indicators (cell numbers, fluorescence intensity, and spike numbers) as seen in Figure 5E, with corresponding moments marked with the same letters.

In summary, LH-3PM enabled us to perform long-term live calcium imaging on a zebrafish epilepsy model. Our findings revealed that prior to seizures, the synchronization degree between neurons was low and the neural coding mode was stable. Post-seizure, there was a significant increase in neuronal synchronization and numerous instances of synchronized discharges, with the neural coding mode deviating from its stable state and exhibiting irregular changes at specific moments. Moreover, we utilized LH-3PM for functional imaging of epileptic-like organoids cultured for 11 weeks (Figure S8), recording spontaneous calcium activities of neurons labeled with Fluo4-AM calcium dye. This study highlights LH-3PM's utility in providing insightful observations into the dynamic neural processes associated with epilepsy.

DISCUSSION

The development of LH-3PM marks a notable advancement in optical imaging for studying small model organisms that can scatter signal light in all directions, like zebrafish and organoids. LH-3PM has an enhanced fluorescence collection efficiency, reaching up to 58% at various depths of diverse samples, which significantly surpasses traditional 3PM equipped with the same long working distance objective.

LH-3PM's ability to reduce photodamage, including photobleaching and phototoxicity, is particularly advantageous for long-term live imaging. This ensures minimal interference with biological samples, making it an invaluable tool for detailed studies in developmental biology, neurobiology, and pathology.

Our design offers the advantages of a long working distance and enhanced signal collection efficiency, making it ideal for specific imaging scenarios. On one hand, when the applications require a larger operating space, such as installing micromanipulation[61] or incubation devices[62] within the imaging system, or ensuring the exclusion of external contamination and interference to the sample, our design is particularly appropriate. On the other hand, for imaging methods that demand high signal collection efficiency, such as calcium imaging and

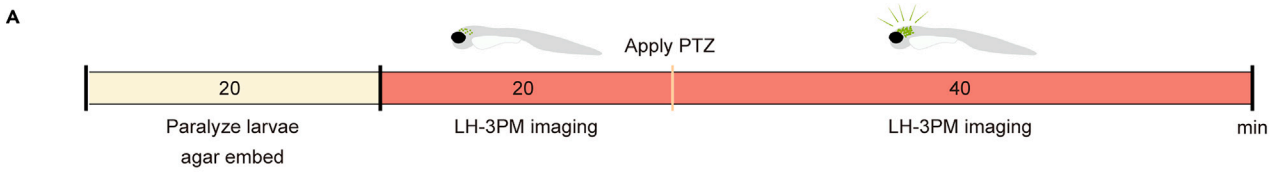
A
Apply PTZ
20
20
40
Paralyze larvae
agar embed
LH-3PM imaging
LH-3PM imaging
min

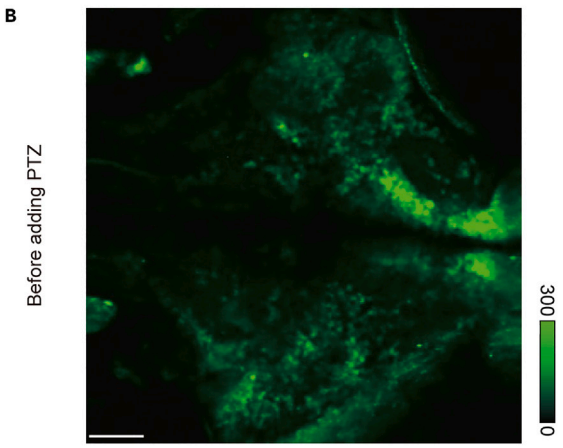
B
Before adding PTZ
300
0

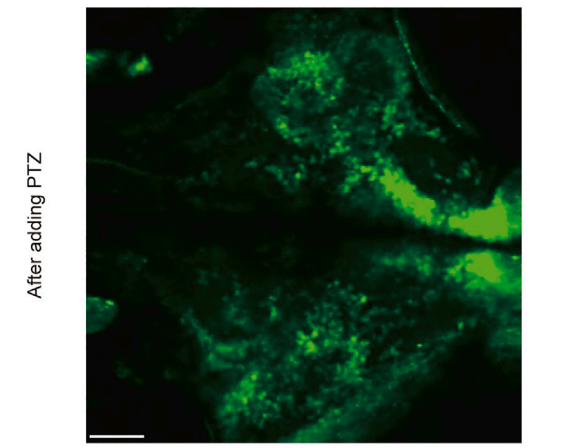
After adding PTZ

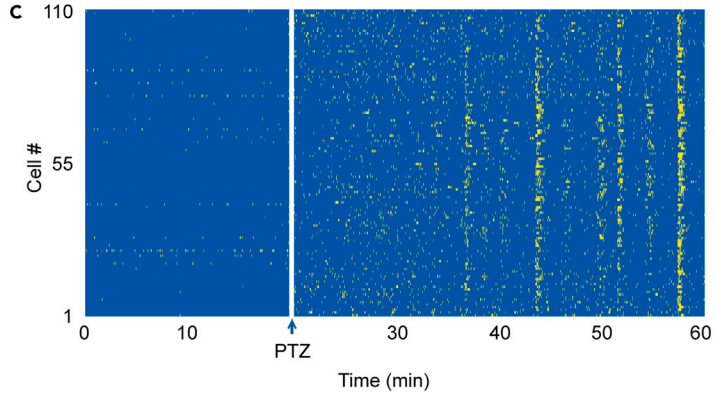
C
110
55
1
Cell #
0
10
30
40
50
60
PTZ
Time (min)

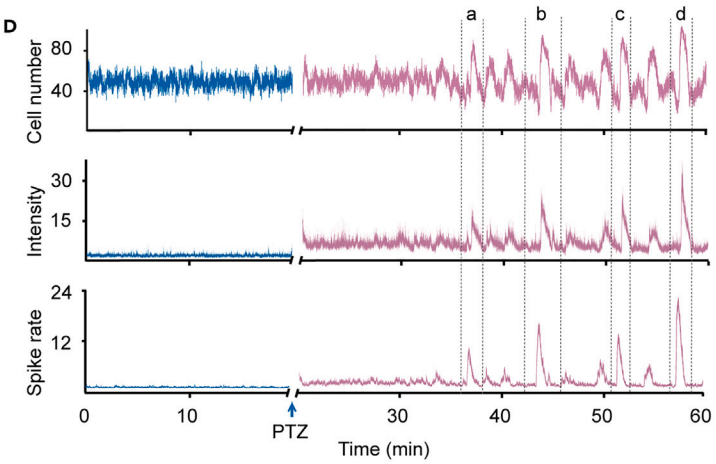
D
a
b
c
d
Cell number
80
40
Intensity
30
15
Spike rate
24
12
0
10
30
40
50
60
PTZ
Time (min)

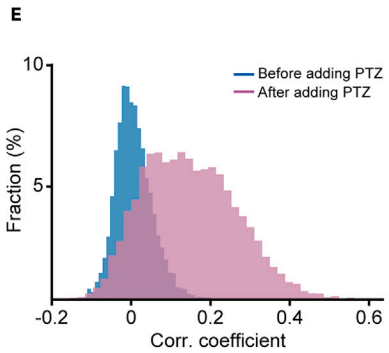
E
Before adding PTZ
After adding PTZ
Fraction (%)
10
5
-0.2
0
0.2
0.4
0.6
Corr. coefficient

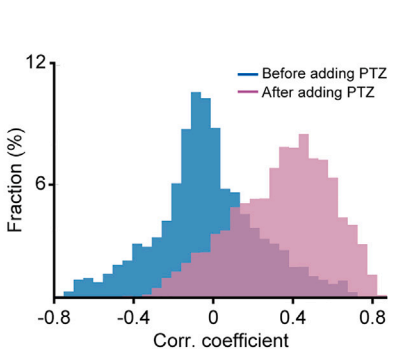
Before adding PTZ
After adding PTZ
Fraction (%)
12
6
-0.8
-0.4
0
0.4
0.8
Corr. coefficient

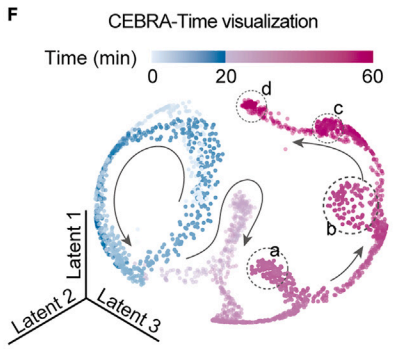
F
CEBRA-Time visualization
Time (min)
0
20
60
d
c
b
a
Latent 1
Latent 2
Latent 3

Figure 5. Long-term neural recording by our LH-3PM reveals the seizure-like activity of zebrafish induced by PTZ

(A) Experimental workflow of zebrafish agar fixation, LH-3PM imaging and drug induction.

(B) Structural image of neurons with LH-3PM before and after adding PTZ.

(C) Map of neuron intensity changes over time, binarized using three times the SEM as a threshold. Addition of PTZ elicit highly synchronized neural activity.

(D) Curves of cell segmentation number, the average fluorescence intensity of spikes and the total number of spikes versus imaging depth.

(E) Distribution of pairwise correlation of mean firing rates across a sliding 1.4-s window (top) and ΔF/F (bottom) before (blue) and after (pink) PTZ administration for GCaMP8f-labeled neurons in zebrafish.

(F) CEBRA-Time (on mean firing rates) 3D visualization of long-term neural recording before (blue) and after (pink) PTZ administration for GCaMP8f-labeled neurons in zebrafish. Scale bars, 50 μm.

especially voltage imaging, where signals are relatively weak and require maximizing signal capture capability, our design will also be advantageous.

In conclusion, LH-3PM presents itself as a significant contribution to optical imaging, enhancing the capabilities for observing complex biological phenomena. Its potential for broader application in various biological research areas offers promising avenues for future exploration and optimization.

Limitations of this study

While LH-3PM marks a notable advancement in imaging small model organisms, its applicability to larger specimens is limited by the size constraints of its internal chamber. In this study, limited by the availability of commercial long working distance objectives, we used a 20× 0.4NA objective from Mitutoyo to validate the feasibility of our design. However, due to its low NA and lack of specific optimization for multiphoton imaging, this objective is not the ideal choice for such applications. If we could utilize a higher NA long working distance objective specifically designed for multiphoton imaging, such as the Cousa objective,[34] the overall imaging performance of our system could be further improved.

Although our design significantly improves the signal light collection efficiency of long working distance objectives, there is still room for further optimization in the light-reflecting chamber. For instance, by replacing the lateral flat mirrors with parabolic mirrors, we observed a further enhancement in the signal light collection efficiency (Figure S9).

Furthermore, LH-3PM's design, being an adaptation of our custom-built microscope, has not fully optimized the optical components, such as the scan and tube lenses, for use with the long working distance objective lens. Our comparison primarily established the viability of LH-3PM against traditional 3PM systems equipped with long working distance objectives. Looking ahead, we anticipate that comprehensive optimization of the system will further enhance LH-3PM's imaging depth and overall performance.

STAR★METHODS

Detailed methods are provided in the online version of this paper and include the following:

- KEY RESOURCES TABLE
- RESOURCE AVAILABILITY
  - Lead contact
  - Materials availability
  - Data and code availability
- EXPERIMENTAL MODEL AND STUDY PARTICIPANT DETAILS
  - Animals
  - Cell lines
- METHOD DETAILS
  - Traditional 3p.m. setup
  - LH-3p.m. setup
  - Simulation of fluorescence distribution in scattering tissues under two-photon and three-photon excitation
  - Simulation of the relationship between the numerical aperture of the objective lens and its photon collection efficiency
  - Zemax simulation of photon collection efficiency
  - Zebrafish sample preparation
  - Mouse brain slice preparation
  - Cortical organoid preparation
  - Comparison of LH-3p.m. and traditional 3p.m.
  - Image processing for structural and functional characterization
  - Calculation of the signal enhancement strength of LH-3p.m.
  - Calculation of the ratio of laser power used by 3p.m. to that of LH-3p.m.
  - Photobleaching and phototoxicity characterization
  - Data analysis of neuronal populations
  - Correlational analysis of functional imaging in PTZ induced zebrafish neuronal populations

- The design and simulation of light-reflecting chambers with lateral parabolic mirrors
- The design and simulation of epi+trans detection

- QUANTIFICATION AND STATISTICAL ANALYSIS

SUPPLEMENTAL INFORMATION

Supplemental information can be found online at https://doi.org/10.1016/j.isci.2024.110554.

ACKNOWLEDGMENTS

We thank Ph.D. student Rong Bao for her guidance on the experiment. We thank Ph.D. student Shilin Fang, Ph.D. student Shan Zhao and Dr. Kui Wang for the construction of the zebrafish line. This work was supported by the National Natural Science Foundation of China (T2222006, 32200951), Science and Technology Commission of Shanghai Municipality (22JC1403100), China Postdoctoral Science Foundation (2022M720801), Shanghai Municipal Science and Technology Major Project, Natural Science Foundation of Shanghai (21ZR1404600), Qiusuo Outstanding Young Talents Program projects: Shanghai Municipal Science and Technology Plan Project (20JC1419500), Shanghai Pilot Program for Basic Research – Fudan University 21TQ1400100 (22TQ019), Fudan University Medical-Engineering Integration Project (Key Project), Brain Science Interdisciplinary Integration Exploration Project - Fudan University MOE Frontiers Center.

AUTHOR CONTRIBUTIONS

B.L. and P.D. designed the study. P.D. carried out the experiments. Y.Z. and P.D. performed theoretical simulations. S.L., P.D., J.H., J.S., and Y.J. performed quantification and statistical analysis. Y.M. and X.Z. provided zebrafish models and performed the experimental operations before imaging. Z.S., Y.K., L.L., J.X., and H.L. provided organoid models and performed the experimental operations before imaging. A.X. performed mouse samples preparation. Y.Z., C.K., Y.X., and S.Y. performed light path calibration. J.W. and X.S. provided mouse models. B.L. and C.K. guided the whole project. B.L., P.D., and S.L. wrote and edited the manuscript. B.L. supported this study financially.

DECLARATION OF INTERESTS

The authors declare that they have no financial or other competing interests.

Received: February 5, 2024
Revised: May 31, 2024
Accepted: July 17, 2024
Published: July 19, 2024

REFERENCES

1. Patton, E.E., Zon, L.I., and Langenau, D.M. (2021). Zebrafish disease models in drug discovery: from preclinical modelling to clinical trials. Nat. Rev. Drug Discov. *20*, 611–628. https://doi.org/10.1038/s41573-021-00210-8.
2. Kim, J., Koo, B.-K., and Knoblich, J.A. (2020). Human organoids: model systems for human biology and medicine. Nat. Rev. Mol. Cell Biol. *21*, 571–584. https://doi.org/10.1038/s41580-020-0259-3.
3. Corsini, N.S., and Knoblich, J.A. (2022). Human organoids: New strategies and methods for analyzing human development and disease. Cell *185*, 2756–2769. https://doi.org/10.1016/j.cell.2022.06.051.
4. Eichmüller, O.L., and Knoblich, J.A. (2022). Human cerebral organoids — a new tool for clinical neurology research. Nat. Rev. Neurol. *18*, 661–680. https://doi.org/10.1038/s41582-022-00723-9.
5. Yamamoto, S., Kanca, O., Wangler, M.F., and Bellen, H.J. (2024). Integrating non-mammalian model organisms in the diagnosis of rare genetic diseases in humans. Nat. Rev. Genet. *25*, 46–60. https://doi.org/10.1038/s41576-023-00633-6.
6. Turrini, L., Roschi, L., de Vito, G., Pavone, F.S., and Vanzi, F. (2023). Imaging Approaches to Investigate Pathophysiological Mechanisms of Brain Disease in Zebrafish. Int. J. Mol. Sci. *24*, 9833. https://doi.org/10.3390/ijms24129833.
7. Dekkers, J.F., Alieva, M., Wellens, L.M., Ariese, H.C.R., Jamieson, P.R., Vonk, A.M., Amatngalim, G.D., Hu, H., Oost, K.C., Snippert, H.J.G., et al. (2019). High-resolution 3D imaging of fixed and cleared organoids. Nat. Protoc. *14*, 1756–1771. https://doi.org/10.1038/s41596-019-0160-8.
8. Burrows, D.R.W., Samarut, É., Liu, J., Baraban, S.C., Richardson, M.P., Meyer, M.P., and Rosch, R.E. (2020). Imaging epilepsy in larval zebrafish. Eur. J. Paediatr. Neurol. *24*, 70–80. https://doi.org/10.1016/j.ejpn.2020.01.006.
9. Saberi, A., Aldenkamp, A.P., Kurniawan, N.A., and Bouten, C.V.C. (2022). In-vitro engineered human cerebral tissues mimic pathological circuit disturbances in 3D. Commun. Biol. *5*, 254. https://doi.org/10.1038/s42003-022-03203-4.
10. Samarasinghe, R.A., Miranda, O.A., Buth, J.E., Mitchell, S., Ferando, I., Watanabe, M., Allison, T.F., Kurdian, A., Fotion, N.N., Gandal, M.J., et al. (2021). Identification of neural oscillations and epileptiform changes in human brain organoids. Nat. Neurosci. *24*, 1488–1500. https://doi.org/10.1038/s41593-021-00906-5.
11. Huang, Q., Garrett, A., Bose, S., Blocker, S., Rios, A.C., Clevers, H., and Shen, X. (2021). The frontier of live tissue imaging across space and time. Cell Stem Cell *28*, 603–622. https://doi.org/10.1016/j.stem.2021.02.010.
12. Hofer, M., and Lutolf, M.P. (2021). Engineering organoids. Nat. Rev. Mater. *6*, 402–420. https://doi.org/10.1038/s41578-021-00279-y.
13. Tallapragada, N.P., Cambra, H.M., Wald, T., Keough Jalbert, S., Abraham, D.M., Klein, O.D., and Klein, A.M. (2021). Inflation-collapse dynamics drive patterning and morphogenesis in intestinal organoids. Cell Stem Cell *28*, 1516–1532.e14. https://doi.org/10.1016/j.stem.2021.04.002.
14. Sharf, T., van der Molen, T., Glasauer, S.M.K., Guzman, E., Buccino, A.P., Luna, G., Cheng, Z., Audouard, M., Ranasinghe, K.G., Kudo, K., et al. (2022). Functional neuronal circuitry and oscillatory dynamics in human brain organoids. Nat. Commun. *13*, 4403. https://doi.org/10.1038/s41467-022-32115-4.
15. Baptista, D., Tahmasebi Birgani, Z., Widowski, H., Passanha, F., Stylianidis, V., Knoops, K., Gubbins, E., Iriondo, C., Skarp, K.-P., Rottier, R.J., et al. (2023). Polymer film-based microwell array platform for long-term culture and research of human bronchial organoids. Mater. Today. Bio *19*, 100603. https://doi.org/10.1016/j.mtbio.2023.100603.
16. Beghin, A., Grenci, G., Sahni, G., Guo, S., Rajendiran, H., Delaire, T., Mohamad Raffi,

S.B., Blanc, D., de Mets, R., Ong, H.T., et al. (2022). Automated high-speed 3D imaging of organoid cultures with multi-scale phenotypic quantification. Nat. Methods *19*, 881–892. https://doi.org/10.1038/s41592-022-01508-0.

17. Horton, N.G., Wang, K., Kobat, D., Clark, C.G., Wise, F.W., Schaffer, C.B., and Xu, C. (2013). *In vivo* three-photon microscopy of subcortical structures within an intact mouse brain. Nat. Photonics *7*, 205–209. https://doi.org/10.1038/nphoton.2012.336.
18. Ouzounov, D.G., Wang, T., Wang, M., Feng, D.D., Horton, N.G., Cruz-Hernández, J.C., Cheng, Y.T., Reimer, J., Tolias, A.S., Nishimura, N., and Xu, C. (2017). In vivo three-photon imaging of activity of GcamP6-labeled neurons deep in intact mouse brain. Nat. Methods *14*, 388–390. https://doi.org/10.1038/nmeth.4183.
19. Li, B., Wu, C., Wang, M., Charan, K., and Xu, C. (2020). An adaptive excitation source for high-speed multiphoton microscopy. Nat. Methods *17*, 163–166. https://doi.org/10.1038/s41592-019-0663-9.
20. Choe, K., Hontani, Y., Wang, T., Hebert, E., Ouzounov, D.G., Lai, K., Singh, A., Béguelin, W., Melnick, A.M., and Xu, C. (2022). Intravital three-photon microscopy allows visualization over the entire depth of mouse lymph nodes. Nat. Immunol. *23*, 330–340. https://doi.org/10.1038/s41590-021-01101-1.
21. Xiao, Y., Deng, P., Zhao, Y., Yang, S., and Li, B. (2023). Three-photon excited fluorescence imaging in neuroscience: From principles to applications. Front. Neurosci. *17*, 1085682. https://doi.org/10.3389/fnins.2023.1085682.
22. Janiak, F.K., Bartel, P., Bale, M.R., Yoshimatsu, T., Komulainen, E., Zhou, M., Staras, K., Prieto-Godino, L.L., Euler, T., Maravall, M., and Baden, T. (2022). Non-telecentric two-photon microscopy for 3D random access mesoscale imaging. Nat. Commun. *13*, 544. https://doi.org/10.1038/s41467-022-28192-0.
23. Yaniv, K., Isogai, S., Castranova, D., Dye, L., Hitomi, J., and Weinstein, B.M. (2006). Live imaging of lymphatic development in the zebrafish. Nat. Med. *12*, 711–716. https://doi.org/10.1038/nm1427.
24. Wee, C.L., Nikitchenko, M., Wang, W.-C., Luks-Morgan, S.J., Song, E., Gagnon, J.A., Randlett, O., Bianco, I.H., Lacoste, A.M.B., Glushenkova, E., et al. (2019). Zebrafish oxytocin neurons drive nocifensive behavior via brainstem premotor targets. Nat. Neurosci. *22*, 1477–1492. https://doi.org/10.1038/s41593-019-0452-x.
25. Lovett-Barron, M., Chen, R., Bradbury, S., Andalman, A.S., Wagle, M., Guo, S., and Deisseroth, K. (2020). Multiple convergent hypothalamus–brainstem circuits drive defensive behavior. Nat. Neurosci. *23*, 959–967. https://doi.org/10.1038/s41593-020-0655-1.
26. Chow, D.M., Sinefeld, D., Kolkman, K.E., Ouzounov, D.G., Akbari, N., Tatarsky, R., Bass, A., Xu, C., and Fetcho, J.R. (2020). Deep three-photon imaging of the brain in intact adult zebrafish. Nat. Methods *17*, 605–608. https://doi.org/10.1038/s41592-020-0819-7.
27. Mansour, A.A., Gonçalves, J.T., Bloyd, C.W., Li, H., Fernandes, S., Quang, D., Johnston, S., Parylak, S.L., Jin, X., and Gage, F.H. (2018). An in vivo model of functional and vascularized human brain organoids. Nat. Biotechnol. *36*, 432–441. https://doi.org/10.1038/nbt.4127.
28. Yildirim, M., Delepine, C., Feldman, D., Pham, V.A., Chou, S., Ip, J., Nott, A., Tsai, L.-H., Ming, G.-L., So, P.T.C., and Sur, M. (2022). Label-free three-photon imaging of intact human cerebral organoids for tracking early events in brain development and deficits in Rett syndrome. Elife *11*, e78079. https://doi.org/10.7554/eLife.78079.
29. Wang, T., and Xu, C. (2020). Three-photon neuronal imaging in deep mouse brain. Optica *7*, 947. https://doi.org/10.1364/OPTICA.395825.
30. Akbari, N., Tatarsky, R.L., Kolkman, K.E., Fetcho, J.R., Bass, A.H., and Xu, C. (2022). Whole-brain optical access in a small adult vertebrate with two- and three-photon microscopy. iScience *25*, 105191. https://doi.org/10.1016/j.isci.2022.105191.
31. Yildirim, M., Sugihara, H., So, P.T.C., and Sur, M. (2019). Functional imaging of visual cortical layers and subplate in awake mice with optimized three-photon microscopy. Nat. Commun. *10*, 177. https://doi.org/10.1038/s41467-018-08179-6.
32. Ferrer Ortas, J., Mahou, P., Escot, S., Stringari, C., David, N.B., Bally-Cuif, L., Dray, N., Négrerie, M., Supatto, W., and Beaurepaire, E. (2023). Label-free imaging of red blood cells and oxygenation with color third-order sum-frequency generation microscopy. Light Sci. Appl. *12*, 29. https://doi.org/10.1038/s41377-022-01064-4.
33. Rodríguez, C., Chen, A., Rivera, J.A., Mohr, M.A., Liang, Y., Natan, R.G., Sun, W., Milkie, D.E., Bifano, T.G., Chen, X., and Ji, N. (2021). An adaptive optics module for deep tissue multiphoton imaging in vivo. Nat. Methods *18*, 1259–1264. https://doi.org/10.1038/s41592-021-01279-0.
34. Yu, C.-H., Yu, Y., Adsit, L.M., Chang, J.T., Barchini, J., Moberly, A.H., Benisty, H., Kim, J., Young, B.K., Heng, K., et al. (2024). The Cousa objective: a long-working distance air objective for multiphoton imaging in vivo. Nat. Methods *21*, 132–141. https://doi.org/10.1038/s41592-023-02098-1.
35. Terada, S.-I., Kobayashi, K., Ohkura, M., Nakai, J., and Matsuzaki, M. (2018). Super-wide-field two-photon imaging with a micro-optical device moving in post-objective space. Nat. Commun. *9*, 3550. https://doi.org/10.1038/s41467-018-06058-8.
36. Barson, D., Hamodi, A.S., Shen, X., Lur, G., Constable, R.T., Cardin, J.A., Crair, M.C., and Higley, M.J. (2020). Simultaneous mesoscopic and two-photon imaging of neuronal activity in cortical circuits. Nat. Methods *17*, 107–113. https://doi.org/10.1038/s41592-019-0625-2.
37. Redman, W.T., Wolcott, N.S., Montelisciani, L., Luna, G., Marks, T.D., Sit, K.K., Yu, C.-H., Smith, S., and Goard, M.J. (2022). Long-term transverse imaging of the hippocampus with glass microperiscopes. Elife *11*, e75391. https://doi.org/10.7554/eLife.75391.
38. Chen, Y., Li, X., Zhang, D., Wang, C., Feng, R., Li, X., Wen, Y., Xu, H., Zhang, X.S., Yang, X., et al. (2020). A Versatile Tiling Light Sheet Microscope for Imaging of Cleared Tissues. Cell Rep. *33*, 108349. https://doi.org/10.1016/j.celrep.2020.108349.
39. Makale, M., McElroy, M., O'Brien, P., Hoffman, R.M., Guo, S., Bouvet, M., Barnes, L., Ingulli, E., and Cheresh, D. (2009). Extended-working-distance multiphoton micromanipulation microscope for deep-penetration imaging in live mice and tissue. J. Biomed. Opt. *14*, 024032. https://doi.org/10.1117/1.3103783.
40. Zinter, J.P., and Levene, M.J. (2011). Maximizing fluorescence collection efficiency in multiphoton microscopy. Opt Express *19*, 15348–15362. https://doi.org/10.1364/OE.19.015348.
41. Wu, Y., Kumar, A., Smith, C., Ardiel, E., Chandris, P., Christensen, R., Rey-Suarez, I., Guo, M., Vishwasrao, H.D., Chen, J., et al. (2017). Reflective imaging improves spatiotemporal resolution and collection efficiency in light sheet microscopy. Nat. Commun. *8*, 1452. https://doi.org/10.1038/s41467-017-01250-8.
42. Combs, C.A., Smirnov, A.V., Riley, J.D., Gandjbakhche, A.H., Knutson, J.R., and Balaban, R.S. (2007). Optimization of multiphoton excitation microscopy by total emission detection using a parabolic light reflector. J. Microsc. *228*, 330–337. https://doi.org/10.1111/j.1365-2818.2007.01851.x.
43. Combs, C.A., Smirnov, A., Chess, D., Mcgavern, D.B., Schroeder, J.L., Riley, J., Kang, S.S., Lugar-Hammer, M., Gandjbakhche, A., Knutson, J.R., and Balaban, R.S. (2011). Optimizing multiphoton fluorescence microscopy light collection from living tissue by noncontact total emission detection (epiTED). J. Microsc. *241*, 153–161. https://doi.org/10.1111/j.1365-2818.2010.03411.x.
44. Combs, C.A., Smirnov, A., Glancy, B., Karamzadeh, N.S., Gandjbakhche, A.H., Redford, G., Kilborn, K., Knutson, J.R., and Balaban, R.S. (2014). Compact non-contact total emission detection for in vivo multiphoton excitation microscopy. J. Microsc. *253*, 83–92. https://doi.org/10.1111/jmi.12099.
45. Zhao, Z., Zhou, Y., Liu, B., He, J., Zhao, J., Cai, Y., Fan, J., Li, X., Wang, Z., Lu, Z., et al. (2023). Two-photon synthetic aperture microscopy for minimally invasive fast 3D imaging of native subcellular behaviors in deep tissue. Cell *186*, 2475–2491.e22. https://doi.org/10.1016/j.cell.2023.04.016.
46. Xu, Y., Liu, N., Bao, X., Liu, B., and Shen, H. (2016). A Quarter Ellipsoidal Reflector Enhancing Fluorescence Collection Efficiency For Multiphoton Microscopes. IEEE Photonics J. *8*, 1–9. https://doi.org/10.1109/JPHOT.2016.2615284.
47. Wang, T., Wu, C., Ouzounov, D.G., Gu, W., Xia, F., Kim, M., Yang, X., Warden, M.R., and Xu, C. (2020). Quantitative analysis of 1300-nm three-photon calcium imaging in the mouse brain. Elife *9*, e53205. https://doi.org/10.7554/eLife.53205.
48. Engelbrecht, C.J., Göbel, W., and Helmchen, F. (2009). Enhanced fluorescence signal in nonlinear microscopy through supplementary fiber-optic light collection. Opt Express *17*, 6421–6435. https://doi.org/10.1364/OE.17.006421.
49. Gauderon, R., Lukins, P.B., and Sheppard, C.J. (1999). Effect of a confocal pinhole in two-photon microscopy. Microsc. Res. Tech. *47*, 210–214. https://doi.org/10.1002/(SICI)1097-0029(19991101)47:3<210::AID-JEMT7>3.0.CO;2-H.
50. Hoebe, R.A., Van Oven, C.H., Gadella, T.W.J., Dhonukshe, P.B., Van Noorden, C.J.F., and Manders, E.M.M. (2007). Controlled light-exposure microscopy reduces photobleaching and phototoxicity in fluorescence live-cell imaging. Nat. Biotechnol. *25*, 249–253. https://doi.org/10.1038/nbt1278.
51. Zhang, X., Dorlhiac, G., Landry, M.P., and Streets, A. (2022). Phototoxic effects of nonlinear optical microscopy on cell cycle, oxidative states, and gene expression. Sci.

Rep. *12*, 18796. https://doi.org/10.1038/s41598-022-23054-7.

52. Laissue, P.P., Alghamdi, R.A., Tomancak, P., Reynaud, E.G., and Shroff, H. (2017). Assessing phototoxicity in live fluorescence imaging. Nat. Methods *14*, 657–661. https://doi.org/10.1038/nmeth.4344.
53. Icha, J., Weber, M., Waters, J.C., and Norden, C. (2017). Phototoxicity in live fluorescence microscopy, and how to avoid it. Bioessays *39*, 1700003. https://doi.org/10.1002/bies.201700003.
54. Pachitariu, M., Stringer, C., Schröder, S., Dipoppa, M., Rossi, L.F., Dalgleish, H., Carandini, M., and Harris, K.D. (2016). Suite2p: beyond 10,000 neurons with standard two-photon microscopy. Preprint at bioRxiv *1*, 061507. https://doi.org/10.1101/061507.
55. Devinsky, O., Vezzani, A., O'Brien, T.J., Jette, N., Scheffer, I.E., de Curtis, M., and Perucca, P. (2018). Epilepsy. Nat. Rev. Dis. Primers *4*, 18024. https://doi.org/10.1038/nrdp.2018.24.
56. Rho, J.M., and Boison, D. (2022). The metabolic basis of epilepsy. Nat. Rev. Neurol. *18*, 333–347. https://doi.org/10.1038/s41582-022-00651-8.
57. Liu, J., and Baraban, S.C. (2019). Network Properties Revealed during Multi-Scale Calcium Imaging of Seizure Activity in Zebrafish. eNeuro *6*, 0041. https://doi.org/10.1523/ENEURO.0041-19.2019.
58. Hasani, H., Sun, J., Zhu, S.I., Rong, Q., Willomitzer, F., Amor, R., McConnell, G., Cossairt, O., and Goodhill, G.J. (2023). Whole-brain imaging of freely-moving zebrafish. Front. Neurosci. *17*, 1127574. https://doi.org/10.3389/fnins.2023.1127574.
59. Baraban, S.C., Taylor, M.R., Castro, P.A., and Baier, H. (2005). Pentylenetetrazole induced changes in zebrafish behavior, neural activity and c-fos expression. Neuroscience *131*, 759–768. https://doi.org/10.1016/j.neuroscience.2004.11.031.
60. Schneider, S., Lee, J.H., and Mathis, M.W. (2023). Learnable latent embeddings for joint behavioural and neural analysis. Nature *617*, 360–368. https://doi.org/10.1038/s41586-023-06031-6.
61. Özelçi, E., Mailand, E., Rüegg, M., Oates, A.C., and Sakar, M.S. (2022). Deconstructing body axis morphogenesis in zebrafish embryos using robot-assisted tissue micromanipulation. Nat. Commun. *13*, 7934. https://doi.org/10.1038/s41467-022-35632-4.
62. Castranova, D., Samasa, B., Venero Galanternik, M., Gore, A.V., Goldstein, A.E., Park, J.S., and Weinstein, B.M. (2022). Long-term imaging of living adult zebrafish. Development *149*, dev199667. https://doi.org/10.1242/dev.199667.
63. Du, X.F., Xu, B., Zhang, Y., Chen, M.J., and Du, J.L. (2018). A transgenic zebrafish model for in vivo long-term imaging of retinotectal synaptogenesis. Sci. Rep. *8*, 14077. https://doi.org/10.1038/s41598-018-32409-y.
64. Shang, C.F., Wang, Y.F., Zhao, M.T., Fan, Q.X., Zhao, S., Qian, Y., Xu, S.J., Mu, Y., Hao, J., and Du, J.L. (2024). Real-time analysis of large-scale neuronal imaging enables closed-loop investigation of neural dynamics. Nat. Neurosci. *27*, 1014–1018. https://doi.org/10.1038/s41593-024-01595-6.
65. Schneider, C.A., Rasband, W.S., and Eliceiri, K.W. (2012). NIH Image to ImageJ: 25 years of image analysis. Nat. Methods *9*, 671–675. https://doi.org/10.1038/nmeth.2089.
66. Chen, C., Qin, Z., He, S., Liu, S., Lau, S.-F., Wu, W., Zhu, D., Ip, N.Y., and Qu, J.Y. (2021). High-resolution two-photon transcranial imaging of brain using direct wavefront sensing. Photonics Res. *9*, 1144. https://doi.org/10.1364/PRJ.420220.
67. Lecoq, J., Oliver, M., Siegle, J.H., Orlova, N., Ledochowitsch, P., and Koch, C. (2021). Removing independent noise in systems neuroscience data using DeepInterpolation. Nat. Methods *18*, 1401–1408. https://doi.org/10.1038/s41592-021-01285-2.

STAR★METHODS

KEY RESOURCES TABLE

REAGENT or RESOURCE	SOURCE	IDENTIFIER
Chemicals, peptides, and recombinant proteins		
Pentylenetetrazole	Sigma-Aldrich	P6500; CAS: 54-95-5
Fluo-4 a.m.	Invitrogen	F14201
Low melting point agarose	Thermofisher Scientific	16520050
Experimental models: cell lines		
Human embryonic stem cell line (H9)	Wicell	Agreement No. 22-W0510
Experimental models: organisms/strains		
Mouse: C57BL/6J	The Jackson Laboratory	JAX# 000664, RRID: IMSR_JAX:000664
Mouse: B6.129P2(Cg)-Cx3cr1tm1Litt/J	The Jackson Laboratory	JAX# 005582, RRID: IMSR_JAX:005582
Zebrafish: Tg(elavl3:GAL4-VP16); Tg(UAS:mGreenLantern)	A gift from Yu Mu Lab	Du et al.[63]
Zebrafish: Tg(elavl3:H2B GCaMP7f)	A gift from Yu Mu Lab	ZDB-TGCONSTRCT-230117-2
Zebrafish: Tg(elavl3:H2B GCaMP8f)	A gift from Yu Mu Lab	Shang et al.[64]
Software and algorithms		
ImageJ	Schneider et al.[65]	https://imagej.net/ij/
MATLAB R2021b	MathWorks	https://www.mathworks.com
Suite2P	https://www.suite2p.org/	https://github.com/MouseLand/suite2p
OpticStudio	Zemax	https://www.zemax.com
Deepinterpolation	https://github.com/AllenInstitute/deepinterpolation	N/A
CEBRA	https://cebra.ai/docs/index.html	https://github.com/AdaptiveMotorControlLab/CEBRA
Other		
20X/0.4 NA Dry objective	Mitutoyo	MY20X-824
Long pass filter	LBTEK	DMR-950LP-C-SP
Photomultiplier tube	Hamamatsu Photonics	H13543-300

RESOURCE AVAILABILITY

Lead contact

Further information and requests for resources and reagents should be directed to and will be fulfilled by the Lead Contact, Bo Li (bo_li@fudan.edu.cn).

Materials availability

This study did not generate new unique reagents.

Data and code availability

- All data reported in this paper will be shared by the lead contact upon request.
- All original code is available in this paper's supplemental information.
- Any additional information required to reanalyze the data reported in this paper is available from the lead contact upon request.

EXPERIMENTAL MODEL AND STUDY PARTICIPANT DETAILS

Animals

All animal experiments were performed according to ethical compliance approved by the Institutional Animal Care and Use Committee of the Department of Laboratory Animal Science at Fudan University (202009001S and 2021JS-NZHY-002).

We used C57BL/6J mice and B6.129P2(Cg)-Cx3cr1tm1Litt/J mice for structural and photobleaching characterization. All of them were purchased from Jackson Lab. For C57BL/6J mice, by injecting (pAAV-CaMKIIα-EGFP-3xFLAG-WPRE) virus into the cortex or BLA brain regions of mice, neurons can be labeled with GFP. For all experiments, 2-3-month-old mice from both sexes were used, no effect of gender was observed in the experiment.

We prepared three types of zebrafish samples, all of which were generously provided by Yu Mu. Zebrafish larvae of Tg(elval3:GAL4-VP16); Tg(UAS:mGreenLantern) line at 5 days post-fertilization (dpf) were used for structural characterization.[63] Zebrafish larvae of Tg(elavl3:H2B GCaMP7f) line at 5 dpf were used for functional characterization. The Tg(elavl3:H2B GCaMP8f) line at 5 dpf were used to construct an acute seizure model.[64] We used both male and female zebrafish in all experiments and no effect of gender was observed in the results.

Cell lines

All the cortical organoids were gifts from Zhicheng Shao. 30-day cortical organoids were induced from the human embryonic stem cell line (H9), which were used for structural characterization. The H9 cell line was obtained from WiCell company (Agreement No. 22-W0510) and cultured in Nutristem medium. 11-week epileptic-like cortical organoids were induced from iPSCs reprogrammed from FCD II patient's somatic cells (patient age and sex: 7 years, female; FCD IIb) and cultured in E8 medium. All the cell lines were cultured in 37°C and 5% CO^2 conditions. No mycoplasma contamination was detected in any cell line.

METHOD DETAILS

Traditional 3p.m. setup

The excitation source at 1300 nm was a noncollinear optical parametric amplifier (I-OPA-TW-F, Light Conversion). The repetition rate of the laser was 1 MHz. A two-prism (SF11 glass) compressor was used to compensate for the normal dispersion of the 1300 nm light source and the microscope, including the objective lens. The images were taken with a custom-built three-photon microscope with a long-working-distance objective (Mitutoyo MY20X-824, 20X, NA0.4). The signal was epicollected through the objective and then reflected by a dichroic beam splitter (FF775-Di01-25x36, Semrock) to the detectors. We used two PMTs with GaAsP photocathodes (H7422P-40, Hamamatsu) for the fluorescence and third-harmonic generation (THG) signals. The optical filters for the fluorescence and THG channels are 520/60 (i.e., transmission wavelength centered at 520 nm with an FWHM of 60 nm) band-pass filter (Semrock) and 447/60 band-pass filter (Semrock), respectively. A dichroic beam splitter (FF458-Di02-25x36, Semrock) is inserted in the signal path at 45° between the two PMTs to separate the THG and fluorescence. The sample chamber is placed on a motorized stage (MP-285A, Sutter Instrument Company). A computer running the ScanImage (Vidrio Technologies) module on MATLAB (MathWorks) software was used to control the stage translation and image acquisition. The PMT current was converted to voltage by transimpedance amplifiers (C12419, Hamamatsu). A galvo-resonant scanner (6215H, Cambridge Technology) was used.

LH-3p.m. setup

The excitation optical path of LH-3p.m. was identical to that of traditional 3p.m., but the fluorescence collection utilized our self-designed light-reflecting chamber. The main body of the chamber was composed of three side reflective mirrors, two bottom long-pass filters (DMR-950LP-C-SP, LBTEK), and one top long-pass filter (DMR-950LP-C-SP, LBTEK). The bottom long-pass filters and mirrors were bonded together with two support bases. The surface of the support base is coated with black paint to absorb any stray excitation light. A PMT (H13543-300, Hamamatsu) with a large rectangular photosensitive area was placed at the light output of the chamber to capture the photon signals reflected from the light-reflecting chamber. The PMT current was converted to voltage by transimpedance amplifiers (C7319, Hamamatsu).

Considering the size of zebrafish and organoid samples, we customized a sample chamber for the light-reflecting chamber, with internal dimensions of 8 × 8.5 mm and a height of 4 mm, and external dimensions of 10 × 12.5 mm with a height of 5 mm. Since we selected a PMT with a photosensitive area of 18 × 18 mm, this roughly limited the side length of the chamber's light output aperture. By adjusting the side length of the light output aperture and the tilt angle of the bottom long-pass filter, we simulated the chamber's light collection path and determined the optimal parameters for collection efficiency (as shown in Figure S1E). The simulation results showed that when the tilt angle of the long pass filter was 45° and the side length was 13 mm, the collection efficiency can reach up to 58%. Based on this, we further determined the dimensions of the other components of the light-reflecting chamber. The dimensions (length×width×height) of the three mirrors were 16.3 × 15 × 2 mm, 16.3 × 15 × 2 mm, and 15 × 13 × 2 mm, respectively. Two bottom long-pass filters were both 8 × 13 × 1 mm. The chamber's bottom consisted of a rectangular fixed base measuring 14.3 × 13 × 1 mm and a right-angled triangular prism fixed base with a side length of 6.3 mm and a height of 13 mm, ensuring a 45-degree tilt angle for the long-pass filter. The surface of the support bases was coated with a matte paint to absorb excess excitation light. The top of the chamber was equipped with a removable long-pass filter (20 × 18 × 1 mm).

Between the light output of the chamber and the PMT, a short-pass filter (FESH0750, Thorlabs) and a band-pass filter (FF01-540/50-25, Semrock for fluorescence signals and FF02-447/60-25, Semrock for THG signals) were placed.

The cost of our design is around $3000, including the manufacturing cost of the collection module and sample chamber is around $950, and the H13543-300 is about $2000.

For structural imaging, we imaged the sample using 1024 × 1024-pixel frame size at 0.9 Hz frame rate. For functional imaging, we imaged the neurons continuously using 512 × 512-pixel frame size at 3.56 Hz frame rate.

Simulation of fluorescence distribution in scattering tissues under two-photon and three-photon excitation

To determine the fluorescence collection demands for both 2 p.m. and 3 p.m. (Figures 1A and 1B), we simulated the fluorescence intensity distribution in 1 mm thick scattering tissues under two-photon and three-photon excitation. We only considered the impact of tissue scattering on laser power.

The transverse profile of the optical intensity of the Gaussian beam with an optical power can be described with a Gaussian function:

$$I(r,z) = \frac{2P}{\pi\omega(z)^2}\exp\left(-2\frac{r^2}{\omega(z)^2}\right).$$

The beam radius $\omega(z)$ varying along the propagation direction can be described mathematically as:

$$\omega(z) = \omega_0\sqrt{1+(z/z_R)^2}.$$

The Rayleigh length Z_R can be described as

$$z_R = \frac{\pi\omega_0^2}{\lambda},$$

where ω_0 is the beam waist where the beam radius is at its minimum.

For two-photon excitation, the excitation wavelength was set at 920 nm, while for three-photon excitation, the excitation wavelength was set at 1300 nm.

Besides, the power of ballistic excitation light decreases exponentially with depth in biological tissue. The excitation power P at the depth z can be described as:

$$P = P_0\exp\left(-\frac{z}{l_e}\right).$$

P_0 is the power at the surface and l_e is the effective attenuation length.

As we simulated the multiphoton excitation in mouse neocortex, the effective attenuation length at 920 nm was set at 150 μm, while the effective attenuation length at 1300 nm was set at 300 μm.[47]

We set the same powers at the surface under two-photon and three-photon excitation. Besides, the signal intensity S of the two-photon excitation is proportional to the square of the excitation intensity I:

$$S \propto I^2.$$

The signal intensity S of the three-photon excitation is proportional to the cube of the excitation intensity I:

$$S \propto I^3.$$

Finally, the fluorescence intensity profiles under two- and three-photon excitation were normalized. By calculating the sum of the signal intensity at the focal point and the sum of the background fluorescence intensity at different imaging depths, we obtained the curve of the signal-to-background ratio with imaging depth under two kinds of nonlinear excitation (Method S1).

Simulation of the relationship between the numerical aperture of the objective lens and its photon collection efficiency

Under the ideal conditions that neglect fluorescence losses caused by sample scattering and refractive index mismatches, we estimated the achievable maximum photon collection efficiency of an objective lens (Figure 1E; Method S2). Assuming a point light source is positioned at the working distance of the objective and emits fluorescence uniformly in all directions, the emitted photons will form a spherical emission distribution. The objective can only collect the fluorescence photons from the spherical crown surface on its same side. By calculating the ratio of the sphere crown area and the corresponding sphere area, we can get the relationship between the maximum collection efficiency of the objective Φ and the half angle of the light cone θ:

$$\Phi = \frac{1-\cos\theta}{2}.$$

The half angle of the light cone can be obtained from the numerical aperture (NA) of the objective lens. An objective's NA is a measure of its angular acceptance for fluorescence light. It is defined as the product of the refractive index of the immersion medium n and the sine of the maximum ray angle against the axis, that is half angle of light cone θ:

$$NA = n\sin\theta.$$

Zemax simulation of photon collection efficiency

Using Zemax software's non-sequential mode, the fluorescence collection optical paths for two methods were constructed and simulated.

An ellipsoidal model of scattering biological tissue was built (semi-axis lengths: 2, 1 and 1 mm). To model human tissue, the Henyey-Greenstein scattering model was employed to define the angular scattering of the rays with a mean path of 0.0894 mm, a transmission of 0.9982, and an anisotropy factor of 0.88.[66] The imaging focus was placed on the short axis of the ellipsoid.

For the traditional method, a paraxial lens was used to simulate a 20X air objective. The fluorescence emitted by the sample was collected by the paraxial lens, narrowed down through a pair of telescopes, and then passed through the short-pass and the band-pass filters before converging on a 5 mm square detector.

For the collection module method, the optical components were arranged according to the design, with an 18 mm square detector placed after the band-pass filter.

An ellipsoidal light source was placed at the focus, with an energy of 1 W and a diameter of 0.1 μm. Rays were traced, and the total power reaching the detector was recorded to calculate the photon collection efficiency.

Zebrafish sample preparation

The zebrafish larvae of structure characterization were anesthetized before embedding while the zebrafish larvae of functional characterization and seizure-like model were paralyzed before embedding. For larvae to be anesthetized, they were soaked in 100 mg/mL α-bungarotoxin for 3 min. For larvae to be paralyzed, they were soaked in 1 mg/mL α-bungarotoxin for 30 s to cut off the synaptic transmission of the neuromuscular junctions. Later, they were immersed in 10 mL water for 20 min.

For sample immobilization, the larvae were mounted in the sample chamber with 1–2% low melting point agarose solution. The position of the zebrafish larva was carefully adjusted before the polymerization of the agarose solution to ensure effective imaging. The sample chamber was filled with water.

For the acute epilepsy model of zebrafish, we first performed 20-min imaging on embedded healthy zebrafish to record their neural activity under normal physiological conditions. Subsequently, we introduced 10 mM PTZ (pentylenetetrazol) into the culture environment to induce epilepsy and continued imaging for another 40 min to monitor and analyze changes in neural activity during epileptic seizures.

Mouse brain slice preparation

Mouse brains containing GFP labeled neurons or GFP labeled microglia were cut into 1 mm thick brain slices using a vibratome. 1 mm thick brain slices were fixed in the sample chamber with low-melting-point agarose solution, ensuring that the chamber is filled with PBS.

Cortical organoid preparation

For structural characterization, 30-day-old cortical organoids were positioned and mounted within the sample chamber with low-melting-point agarose solution, ensuring that the chamber was filled with the culture medium.

For functional characterization, the cortical organoids were incubated with 2 μg/mL Fluo-4 a.m., a calcium-sensitive dye, for 30 min, and then the dye was washed off with culture medium. The cortical organoids were positioned in the sample chamber and embedded with low-melting-point agarose solution. The chamber was completely filled with the culture medium before imaging.

Comparison of LH-3p.m. and traditional 3p.m.

Both LH-3p.m. and traditional 3p.m. utilized the same long working distance objective (Mitutoyo MY20X-824, 20X, NA0.4) to excite the samples. In all comparative experiments, we employed two methods to image the same area of the sample sequentially. Initially, the sample was placed in the sample chamber, which was then placed inside the light-reflecting chamber. After the sample was imaged by LH-3p.m., the light-reflecting chamber was removed, and the same field of view was imaged with the traditional 3p.m. Through this experimental procedure, we compared the imaging quality of the two methods. To ensure the accuracy of the comparison, we also confirmed that the order of imaging with LH-3p.m. and 3p.m. does not affect the experimental results. Performing traditional 3p.m. imaging of the sample first, followed by LH-3p.m. imaging of the same area, will yield consistent experimental results.

Image processing for structural and functional characterization

All images were filtered to remove the ripple noise from PMT. To display the absolute signal strength in the unit of photon count, pixel values of the images captured by 3p.m. and LH-3p.m. are respectively divided by different calibration factors. The calibration factor is determined by both the PMT's quantum efficiency and the gray value produced after responding to a single photon. First, using the radiative sensitivity-wavelength curve provided in the product sheet of PMT, we can calculate the quantum efficiency of the two methods at the specific wavelength. Then we determined the gray value generated by the two configurations after responding to a single photon. We imaged a uniform fluorescent solution using both methods, controlling the power to ensure that only a single or zero photon is excited in each pixel. The histogram of the gray values of 300 images is shown in the Figure S3. The horizontal axis represents the gray value of a single pixel, and the vertical axis represents the number of pixels. It can be seen that the number of lower pixel values on the left side of the histogram is very high, which is due to the ripple noise of the PMT. By fitting the acquired histogram, we found that the overall distribution of gray values produced after the PMT responded to a single photon is consistent with a Poisson distribution, which aligns with our conjecture, as the phenomenon of the PMT responding to a single photon indeed follows a Poisson distribution. With this method, we were able to determine the gray values outputted after responding to a single photon for the two methods as 931 and 385, respectively. Taking the 520 nm signal as an

example, the calibration factor for LH-3p.m. is 20% × 3.85, while the calibration factor for traditional 3p.m. is 38% × 9.31. After dividing the acquired images by their respective calibration factors, one can eliminate the interference caused by different PMT quantum efficiencies and ensure that a gray value of 100 corresponds to one photon.

Calculation of the signal enhancement strength of LH-3p.m.

For signal enhancement factor in Figure 2E, we identified the same neuronal region in the images captured by 3p.m. and LH-3p.m. The total photon numbers within the neuronal region were calculated. We divided the photon number collected by LH-3p.m. by that collected by 3p.m. to determine the signal enhancement factor.

For signal enhancement factor in Figure 2G, the same region was captured by both 3p.m. and LH-3p.m., and the total photon number of the entire image was calculated. The photon numbers collected by LH-3p.m. were divided by the numbers of photon collected by 3p.m. to determine the signal enhancement factor.

Calculation of the ratio of laser power used by 3p.m. to that of LH-3p.m.

Ensuring that the signal intensities captured by 3p.m. and LH-3p.m. were approximately same, we identified the same neuronal region and calculated the total photon number within the region. The measured power under the objective was divided by photon number to obtain the power value per photon. Then we divided the power value per photon of 3p.m. by that of LH-3p.m. to obtain the power ratio.

Photobleaching and phototoxicity characterization

We characterized the photobleaching and phototoxicity separately.

To characterize photobleaching, brain slices were imaged using both LH-3p.m. and conventional 3p.m., with appropriate power settings to ensure that the initial image signals were essentially consistent. After identifying distinct neuronal structures in the images, the total number of photons from neurons in each frame was calculated, and a curve depicting the change in photon count over time was plotted (Figure 3D). The sum of grayscale values in the rectangular area marked by the white dashed line in each frame was normalized, resulting in a curve showing the change in normalized fluorescence intensity over time (Figure 3E). We used the curve fitting toolbox in MATLAB to fit the fluorescence decay curves separately. The resulting fluorescence decay function for 3p.m. was "y = 5834exp(-0.003649x) + 7306exp(-2.274E-4x)," while for LH-3p.m., it was "y = 408.7exp(-0.01115x) + 13080exp(-1.184E-6x)." Here, "x" represents time, and "y" represents the photon count per frame. Then, we used the bisection method to determine the half-life of the function, i.e., the time for the photon count to halve, finding the half-life for LH-3p.m. to be 559441.7 s, and for 3p.m., 738.7 s. Dividing the two, we concluded that the rate of photobleaching was reduced by 757 times. Through this comparison, we can assess the differences in photobleaching effects on samples between LH-3p.m. and conventional 3p.m.

To characterize phototoxicity, functional imaging of neuronal activity in zebrafish was performed using both LH-3p.m. and conventional 3p.m., with appropriate power to ensure that the initial image signals were essentially consistent. The z stack Depth ColorCode plugin in ImageJ[65] was used to project the obtained time-series images (Figure 3F). The total number of photons contained in each frame was calculated to produce curves showing the change in photon count over time used by the two methods (Figure 3H). We manually segmented the bubble-like damage areas in the images and calculated the proportion of the damaged area by dividing the area of the damage by the total imaging area, to obtain a curve showing the change in the proportion of the damaged area over imaging time (Figure 3I).

Data analysis of neuronal populations

Calcium imaging data of neuronal populations were first registered with a rigid motion correction method. Then, Suite2p was employed as the source extraction method for neuron segmentation and trace extraction.[54] The same set of parameters was used for the LH-3p.m. and traditional 3p.m. A spatial matrix and a temporal matrix can be obtained from each video, representing the spatial footprints and corresponding calcium traces of all active neurons, respectively. OASIS algorithm was used for spike inference of all traces. The baseline fluorescence intensity F_0 of calcium traces was defined as an average of 10%–50% of all fluorescence signals. Thus, the $\Delta F/F_0$ of calcium traces was defined as $(F\text{-}F_0)/F_0$, F: fluorescence intensity of calcium traces over time.

Correlational analysis of functional imaging in PTZ induced zebrafish neuronal populations

In Figure 5, the LH-3p.m. imaging data were first denoised by the Deepinterpolation algorithm to improve the signal-to-noise ratio of calcium traces.[67] Each cell's spike rate curve was estimated by sliding a rectangular window (of 1.4s) along the spike trains of calcium traces. Pairwise correlation coefficients of spike rate curves in Figure 5F were calculated. CEBRA algorithm on only neural data was employed to capture the latent embeddings of all neuronal spike activities.[60] The number of latent variables was set to three.

In the data processing for method comparisons presented in Figures 1, 2, 3, and 4, we did not employ any deep learning algorithms. These were only used in the final application depicted in Figure 5, where method comparison is not involved.

The design and simulation of light-reflecting chambers with lateral parabolic mirrors

We used Solidworks software to design two types of light-reflecting chambers with lateral parabolic mirrors. The lateral parabolic surfaces were generated by the "equation-driven curve" function. The parabolic equation was determined based on the principle that the focus is

at the initial imaging point as 'y2 = 22*x'. Further, we obtained two types of light-reflecting chambers with lateral parabolic surfaces (A) and (B) through stretch cutting (Figure S9A) and rotational cutting (Figure S9B). Then, we simulated the designs using Zemax optical simulation software and calculated their signal collection efficiencies. Figures S9C and S9D show the ray tracing trajectories of photon collection by the two types of lateral parabolic reflectors, and Figure S9E shows the ray tracing trajectory of photon collection by a lateral flat reflector. We calculated the photon collection efficiency at different depths for each method. The results show that as the imaging depth increases, the photon collection efficiency of the three methods remains stable (Figure S9F), and there is no significant difference in photon collection efficiency between the two parabolic mirrors (Lateral parabolic mirror(A): mean ± SEM = 63.57% ± 0.75, Lateral parabolic mirror(B): mean ± SEM = 63.92% ± 0.55). By discussing the design and performance simulation, we found that compared to the light-reflecting chamber design in the main text, changing the sides to two different parabolic shapes can indeed further enhance the overall design, resulting in an increase in signal collection efficiency to 1.09 ± 0.02 and 1.10 ± 0.01 times, respectively.

The design and simulation of epi+trans detection

There are many methods to enhance the fluorescence collection efficiency (Table S1). We found that using epi+trans detection can also get the good collection effective. Epi detection can be achieved by the objective and trans detection can be achieved by the condenser located under the sample stage.

We used optical simulation software to simulate this detection method. Given our design's sample chamber depth of 4 mm, we respectively chose a 1 NA, 4 mm working distance 25X objective (Olympus, XLPLN25XSVMP2) and a 0.4 NA, 20 mm working distance 20X objective (Mitutoyo, MY20X-824) for epi detection. Both condenser and objectives were simulated using paraxial lenses. We employed an oil immersion condenser with a 1.3 NA and an 8.4 mm focal length (Nikon, No. 465253) to achieve trans detection. Epi and trans detection were achieved by setting up a detector rectangle with X and Y half-widths of 9 mm each. We used the detector rectangle to simulate a large-area photomultiplier tube (Hamamatsu, H13543-300). Oil was used as the immersion medium for the condenser. Therefore, we set up a rectangular volume body with a refractive index of 1.51 between the sample chamber and the paraxial lens replacing the condenser to represent the oil. As shown in Figures S10A and S10B, the epi+trans method can collect photons emitted upwards and downwards from the sample but has difficulty collecting signal photons emitted laterally from the sample. The overall setup for epi+trans detection is shown in Figure S10C.

We calculated the photon collection efficiency of three methods at different depths. As shown in Figure S10D, the photon collection efficiency of all three methods remained stable as imaging depth increased. The epi+trans method using a low NA objective achieved a collection efficiency of 29.31% ± 0.32 (mean ± SEM), while the epi+trans method using a high NA objective reached 44.36% ± 0.65 (mean ± SEM).

QUANTIFICATION AND STATISTICAL ANALYSIS

Data were represented as mean values with SEM obtained using MATLAB (MathWorks) software. Statistical significance was determined using one-way ANOVA with the Dunnett's multiple comparisons test. $^{**}p < 0.01$; $^{***}p < 0.001$. Further statistical details, including exact value of n and what n represents, are provided in the figure legends.